

# A Riemann ghost fluid method for the GPR model of continuum mechanics

Haran Jackson<sup>a,\*\*</sup>, Nikos Nikiforakis<sup>a</sup>

<sup>a</sup>*Cavendish Laboratory, JJ Thomson Ave, Cambridge, UK, CB3 0HE*

---

## Abstract

The Godunov-Peshkov-Romenski model of continuum mechanics is claimed to be capable of describing both solids and fluids (both viscous and inviscid) in the same framework [33? ]. Different solids and fluids are governed by the same set of partial differential equations, differing only in their equations of states and strain dissipation functions. This has the potential to streamline development of simulation software for scenarios involving multiple materials and phases of matter, by reducing the number of different systems of equations that require solvers, and cutting down on the amount of theoretical work required.

At present, there is no way of dealing with material interfaces in the GPR model, however. In this study, a modification of Barton’s [3] application of Sambasivan and Udaykumar’s Riemann Ghost Fluid Method [40, 41] is devised for the GPR model, enabling the simulation of material interfaces. This new method is tested on a variety of interface problems. It is demonstrated to accurately reproduce analytical results for known Riemann problems, and to produce expected results with regards to heat conduction across interfaces.

*Keywords:* Godunov-Peshkov-Romenski, GPR, Ghost Fluid Method, RGFM, multimaterial

---

## 1. Background

### 1.1. Multimaterial and Multiphase Models

The definition of a multiphase system is slightly ambiguous in the literature. Here it will be taken to mean a system consisting of either two or more different materials (possibly in the same phase of matter), or two or more volumes of (possibly the same) material in different phases of matter. There are two aspects of multiphase systems that require attention: multiphase flow, and multiphase heat transfer. The latter becomes important when the phases are at different temperatures. In this study, the different phases will be assumed to be immiscible.

Without a unified model of continuum mechanics, capable of describing all phases in the same framework, different sets of equations may have to be used in the different regions occupied by different phases. These systems arise, for example, in fluid-structure interaction, or oil-water interfaces. An overview of current approaches to multiphase systems will now be given. The examples here are illustrative but not exhaustive.

There has been a huge amount of research activity in the field over the years, but current approaches can be broadly classified as either monolithic or partitioned [20]. In a monolithic scheme, all phases are described by the same set of nonlinear equations. The evolution of the interfaces is implicit to the equations, unlike in partitioned schemes. See for example [30, 22]. The system is solved by a multivariate Newton-type method.

---

\*Corresponding author

\*\*Principal corresponding author

Email address: [hj305@cam.ac.uk](mailto:hj305@cam.ac.uk) (Haran Jackson)

It is often ill-conditioned, due to the different scales of the state variables of the different phases. Thus, iterative solvers are required, proving inefficient unless good preconditioners are available. Codes tend to be very specialized to the specific problems they solve, and it requires expertise to develop and maintain such methods.

In a partitioned scheme, the states of the different phases are calculated separately at each time step, possibly using different models. See Rossi and Oñate [38] for a recent overview of some of the common algorithmic features of these schemes. The individual systems do not suffer from the scaling-induced conditioning problems of monolithic schemes, but attention now needs to be paid to the material interfaces. Modeling them can be unstable and relatively computationally expensive (although typically not as expensive as solving the full monolithic systems). One of the great benefits of partitioned schemes is that legacy implementations of common models may be used in the domains occupied by materials that they describe. These implementations are often well-used and relatively bug free, and tend to be written efficiently for the kinds of problems that the solve. As an example of a software suite taking advantage of this, see the Caltech's Virtual Test Facility [1].

Under both types of schemes, the models describing the different phases may be formulated in either a Lagrangian, an Eulerian, or an ALE framework. Solids models tend to come in Lagrangian form, and often these are combined with ALE forms for the fluid phases, so that the fluid meshes may deform to match the deformation of the solid (see, for example, Pin et al. [34]). These schemes tend to be very accurate, but like all Lagrangian schemes, they fail if the meshes become highly contorted. Thus, adaptive remeshing is often necessary. Some authors have coupled a Lagrangian solid scheme with an Eulerian fluid scheme, but extra care must be taken when applying the boundary conditions to the interface, which corresponds to the intersection of the Eulerian and Lagrangian meshes (see Legay et al. [23] for an implementation using level sets, or Fedkiw [14] for a GFM coupling). Some authors, such as Ryzhakov et al. [39], have found success in using the common Lagrangian formulations for the solid, and a reformulated Lagrangian model for the fluid, implementing the necessary adaptive remeshing. Yet another option is to model both the fluid and the solid in an Eulerian framework, although this now necessitates a level set method or volume of fluid method [19] to track the interfaces. Also, these methods are more prone to losing small-scale geometric features of the media, unless methods such as AMR are employed to combat this [20].

In a recently submitted paper, Michael and Nikiforakis [28] (building on the work of Schoch et al. [42]) couple various Eulerian models of reactive and inert fluids and solids by use of a Riemann Ghost Fluid Method, with the ghost states calculated using specialised mixed-material Riemann solvers for each interaction (see Section 1.3). Whilst these techniques do not suffer from the mesh contortion issues inherent in Lagrangian formulations of continuum mechanics, and the interface coupling tends to be less computationally expensive than the iterative techniques demanded by monolithic schemes, a fair amount of theoretical work needs to be done to derive analytical relations describing the interactions between every pair of models used.

If it were possible to describe all phases with the same Eulerian model, this method could be used, with only one type of Riemann solver needed to cope with any multiphase problem posed. This would effectively be a partitioned scheme with the same system solved in each domain. The GPR model represents such an opportunity. As will be seen, the model also includes terms for heat conduction, which do not appear in the basic formulations of many of the common models used in multiphase systems (e.g. the Euler equations, or the Navier-Stokes equations). Heat conduction is often ignored in multiphase modeling, but such a framework based on the GPR model would almost unavoidably include it. It should be noted, though, that any unified model of continuum mechanics purporting to describe all phases of interest must be at least as descriptive as competing models tailored to each individual phase if the utmost model fidelity is required. Although the results for the GPR model applied to standard test cases have been promising, both here and in other preliminary studies [? 8], more work is required to determine how faithfully the GPR model reproduces common agreed phenomenological results.

### 1.2. The Model of Godunov, Peshkov and Romenski

The GPR model, first introduced by Peshkov and Romenski [33] and expanded upon by Dumbser et al. [?], takes the following form:

$$\frac{\partial \rho}{\partial t} + \frac{\partial (\rho v_k)}{\partial x_k} = 0 \quad (1a)$$

$$\frac{\partial (\rho v_i)}{\partial t} + \frac{\partial (\rho v_i v_k + p \delta_{ik} - \sigma_{ik})}{\partial x_k} = 0 \quad (1b)$$

$$\frac{\partial A_{ij}}{\partial t} + \frac{\partial (A_{ik} v_k)}{\partial x_j} + v_k \left( \frac{\partial A_{ij}}{\partial x_k} - \frac{\partial A_{ik}}{\partial x_j} \right) = -\frac{\psi_{ij}}{\theta_1(\tau_1)} \quad (1c)$$

$$\frac{\partial (\rho J_i)}{\partial t} + \frac{\partial (\rho J_i v_k + T \delta_{ik})}{\partial x_k} = -\frac{\rho H_i}{\theta_2(\tau_2)} \quad (1d)$$

$$\frac{\partial (\rho E)}{\partial t} + \frac{\partial (\rho E v_k + (p \delta_{ik} - \sigma_{ik}) v_i + q_k)}{\partial x_k} = 0 \quad (1e)$$

where  $\theta_1$  and  $\theta_2$  are positive scalar functions, and  $\psi = \frac{\partial E}{\partial A}$  and  $\mathbf{H} = \frac{\partial E}{\partial \mathbf{J}}$ . Note that (1a), (1b), (1c), (1d), (1e) can be written in the following form:

$$\frac{\partial \mathbf{Q}}{\partial t} + \nabla \cdot \mathbf{F} + \mathbf{B} \cdot \nabla \mathbf{Q} = \mathbf{S} \quad (2)$$

The following definitions are given:

$$p = \rho^2 \frac{\partial E}{\partial \rho} \quad (3a)$$

$$\sigma = -\rho A^T \frac{\partial E}{\partial A} \quad (3b)$$

$$T = \frac{\partial E}{\partial s} \quad (3c)$$

$$\mathbf{q} = \frac{\partial E}{\partial s} \frac{\partial E}{\partial \mathbf{J}} \quad (3d)$$

To close the system, the EOS must be specified, from which the above quantities and the sources can be derived.  $E$  is the sum of the contributions of the energies at the molecular scale (microscale), the material element<sup>1</sup> scale (mesoscale), and the flow scale (macroscale):

$$E = E_1(\rho, s) + E_2(A, \mathbf{J}) + E_3(\mathbf{v}) \quad (4)$$

In this study,  $E_1$  is taken to correspond to an ideal or stiffened gas:

$$E_1 = \frac{p + \gamma p_\infty}{(\gamma - 1) \rho} \quad (5)$$

where  $p_\infty = 0$  for an ideal gas. The temperature is given by:

---

<sup>1</sup>The concept of a *material element* corresponds to that of a fluid parcel from fluid dynamics, applied to both fluids and solids.

$$T = \frac{p + p_\infty}{(\gamma - 1) c_v \rho} \quad (6)$$

and the speed of sound by:

$$c_0 = \sqrt{\frac{\gamma (p + p_\infty)}{\rho}} \quad (7)$$

It should be noted that there are many other choices that can be made for  $E_1$ , dependent on the type of material being modelled.

$E_2$  is chosen to have the following quadratic form:

$$E_2 = \frac{c_s^2}{4} \|\text{dev}(G)\|_F^2 + \frac{\alpha^2}{2} \|\mathbf{J}\|^2 \quad (8)$$

$\alpha$  is a constant related to the characteristic velocity of propagation of heat waves:

$$c_h = \frac{\alpha}{\rho} \sqrt{\frac{T}{c_v}} \quad (9)$$

$G = A^T A$  is the Gramian matrix of the distortion tensor, and  $\text{dev}(G)$  is the deviator (trace-free part) of  $G$ :

$$\text{dev}(G) = G - \frac{1}{3} \text{tr}(G) I \quad (10)$$

$E_3$  is the usual specific kinetic energy per unit mass:

$$E_3 = \frac{1}{2} \|\mathbf{v}\|^2 \quad (11)$$

The following forms are chosen:

$$\begin{cases} \theta_1(\tau_1) = \frac{\tau_1 c_s^2}{3|A|^{\frac{5}{3}}} & \tau_1 = \frac{6\mu}{\rho_0 c_s^2} \\ \theta_2(\tau_2) = \tau_2 \alpha^2 \frac{\rho T_0}{\rho_0 T} & \tau_2 = \frac{\rho_0 \kappa}{T_0 \alpha^2} \end{cases} \quad (12)$$

The justification of these choices is that classical Navier–Stokes–Fourier theory is recovered in the stiff limit  $\tau_1, \tau_2 \rightarrow 0$  [? ]. This results in the following relations:

$$\sigma = -\rho c_s^2 G \text{dev}(G) \quad (13a)$$

$$\mathbf{q} = \alpha^2 T \mathbf{J} \quad (13b)$$

$$-\frac{\psi}{\theta_1(\tau_1)} = -\frac{3}{\tau_1} |A|^{\frac{5}{3}} A \text{dev}(G) \quad (13c)$$

$$-\frac{\rho \mathbf{H}}{\theta_2(\tau_2)} = -\frac{T \rho_0}{T_0 \tau_2} \mathbf{J} \quad (13d)$$

The following constraint also holds [33]:

$$\det(A) = \frac{\rho}{\rho_0} \quad (14)$$

The model as presented here is the same in structure as Godunov and Romenski's 1970s model of elastoplastic deformation [17]. The differences between the two models lie in the interpretation of the equations in the GPR framework as those governing an arbitrary continuum - not just a solid - and the inclusion of thermal conduction by the evolution of  $\mathbf{J}$ . Unlike in previous continuum models, material elements have not only finite size, but also internal structure.

The strain dissipation time  $\tau_1$  of the GPR model is a continuous analogue of Frenkel's "particle settled life time" [15]; the characteristic time taken for a particle to move by a distance of the same order of magnitude as the particle's size. Thus,  $\tau_1$  characterizes the time taken for a material element to rearrange with its neighbors.  $\tau_1 = \infty$  for solids and  $\tau_1 = 0$  for inviscid fluids. It is in this way that the GPR model seeks to describe all three major phases of matter, as long as a continuum description is appropriate for the material at hand.

The evolution equation for  $\mathbf{J}$  and its contribution to the energy of the system are derived from Romenski's model of hyperbolic heat transfer, originally proposed in [27, 37] and implemented in [36, 35]. In this model,  $\mathbf{J}$  is effectively defined as the variable conjugate to the entropy flux, in the sense that the latter is the derivative of the specific internal energy with respect to  $\mathbf{J}$ . Romenski remarks that it is more convenient to evolve  $\mathbf{J}$  and  $E$  than the heat flux or the entropy flux, and thus the equations take the form given here.  $\mathbf{J}$  can intuitively be thought of as a thermal analogue of momentum.  $\tau_2$  characterizes the speed of relaxation of the thermal impulse due to heat exchange between material elements.

### 1.3. Ghost Fluid Methods

Ghost fluid methods, combined with level set methods, are used to model the evolution of interfaces between different materials. They are detailed here, as it is with such a method that this study proposes to model the interfaces between different materials described by the GPR model.

#### 1.3.1. Level Set Methods

Given a function  $f$  on  $\mathbb{R}$ , the level set of  $f$  at level  $c$  is defined as:

$$\Gamma_c = \{x : f(x) = c\} \quad (15)$$

Given velocity field  $v : \mathbb{R} \rightarrow \mathbb{R}$ ,  $f$  is advected according to the level set equation [32]:

$$\frac{\partial f}{\partial t} = v \left| \frac{\partial f}{\partial x} \right| \quad (16)$$

The advection of a point in a fluid with velocity  $v$  can be modeled by taking  $f = x - x_0$  where  $x_0$  is the position of the point at time  $t = 0$ , and tracking  $\Gamma_0$ . (16) is solved by an appropriate numerical method. The numerical methods used in this study are described in Chapter 2.  $f$  will usually have to be renormalized to resemble a straight line at every time step, to avoid unwanted distortions such as becoming a multivalued function.

#### 1.3.2. The Original Ghost Fluid Method

The Original Ghost Fluid Method of Fedkiw et al. [13] (an adaptation of the work of Glimm et al. [16]) is a numerical method for the Euler equations for simulating interfaces between multiple materials. The primitive variables for the Euler equations in 1D are given by  $\mathbf{P} = \begin{pmatrix} \rho & v & p \end{pmatrix}^T$ .

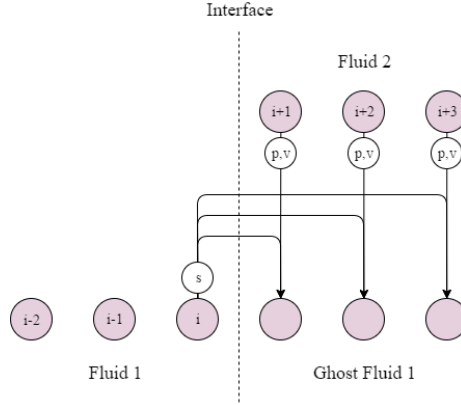


Figure 1: The Original Ghost Fluid Method

Suppose the interface between two fluids is modeled on spatial domain  $[0, 1]$ , divided into  $N$  cells with width  $\Delta x = \frac{1}{N}$ . Let the time step be  $\Delta t$  and let  $\mathbf{P}_i^n$  be the set of primitive variables in cell  $i$  at time  $t_n = n\Delta t$ . Let the level set function  $f$  have root  $x_n$  where  $x_n \in [(i + \frac{1}{2})\Delta x, (i + \frac{3}{2})\Delta x]$ . Thus, at time  $t_n$  the interface lies between the cells with primitive variables  $\mathbf{P}_i^n, \mathbf{P}_{i+1}^n$ . Define two sets of primitive variables:

$$\mathbf{P}_j^{(1)} = \begin{cases} \mathbf{P}_j^n & j \leq i \\ \left( \rho(s_i^n, p_j^n, \gamma_i^n) \quad v_j^n \quad p_j^n \right) & j > i \end{cases} \quad (17)$$

$$\mathbf{P}_j^{(2)} = \begin{cases} \mathbf{P}_j^n & j \geq i+1 \\ \left( \rho(s_{i+1}^n, p_j^n, \gamma_{i+1}^n) \quad v_j^n \quad p_j^n \right) & j < i+1 \end{cases} \quad (18)$$

where:

$$\rho(s, p, \gamma) = \left( \frac{p}{s} \right)^{\frac{1}{\gamma}} \quad (19)$$

All cells in  $\mathbf{P}^{(1)}$  to the left of the interface have the same state variables as those of  $\mathbf{P}^n$ . All cells to the right have the same pressure and velocity as their counterparts in  $\mathbf{P}^n$ , but the same entropy as  $\mathbf{P}_i^n$ . This affects their density. The situation is analogous for  $\mathbf{P}^{(2)}$ . This is demonstrated in Figure 1 on page 6.

$\mathbf{P}^{(1)}, \mathbf{P}^{(2)}$  are stepped forward by time step  $\Delta t$  using a standard Eulerian method.  $f$  is advected using (16), taking the velocity in each cell to be that of  $\mathbf{P}^n$ . Now let  $f(x_{n+1}) = 0$  where  $x_{n+1} \in [(k + \frac{1}{2})\Delta x, (k + \frac{3}{2})\Delta x]$  for some  $k$ . Define:

$$\mathbf{P}_j^{n+1} = \begin{cases} \mathbf{P}_j^{(1)} & j \leq k \\ \mathbf{P}_j^{(2)} & j > k \end{cases} \quad (20)$$

The rationale behind the original GFM is that in most applications, pressure and velocity are continuous across the interface, and thus the ghost cells may take the real pressure and velocity values. Entropy is generally discontinuous at a contact discontinuity, resulting in large truncation errors if a standard finite difference scheme is used to solve the system. Thus, entropy is extrapolated as a constant from the interface boundary cell into the ghost region.

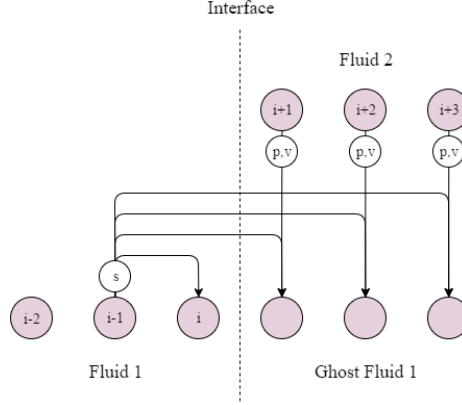


Figure 2: The Original Ghost Fluid Method, with the isobaric fix

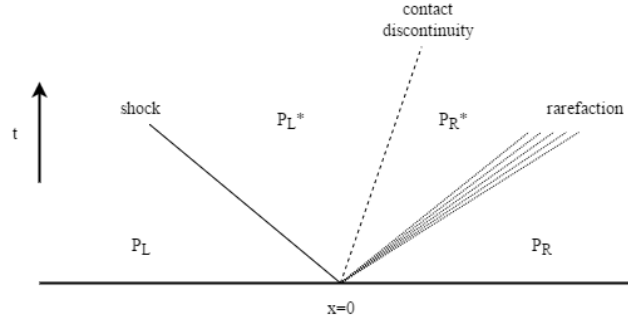


Figure 3: The qualitative structure of the solution to the Riemann Problem, showing the different possible types of waves

Fedkiw et al. advised to use the *isobaric fix* technique. This involves setting the entropy of cell  $i$ , and all cells in the right ghost region, to that of cell  $i - 1$ , and setting the entropy of cell  $i + 1$ , and all cells in the left ghost region, to that of cell  $i + 2$ . This is demonstrated in Figure 2 on page 7.

Effectively, the ghost regions behave like they are composed of the same fluid as the regions they extend (as they have the same entropy), facilitating calculation of the next time step, but they have the same pressure and velocity profiles as the real fluids they replace, meaning the boundary conditions at the interface are upheld.

### 1.3.3. The Riemann Ghost Fluid Method

The Riemann Problem in its general form is the solution of the following initial value problem. Given a set of variables  $\mathbf{P}$  dependent on space and time, and a hyperbolic set of equations which govern their spatio-temporal evolution,  $\mathbf{P}(x, t)$  is sought for  $t > 0$ , given the initial condition:

$$\mathbf{P}(x, 0) = \begin{cases} \mathbf{P}_L & x < 0 \\ \mathbf{P}_R & x > 0 \end{cases} \quad (21)$$

This problem is denoted by  $RP(\mathbf{P}_L, \mathbf{P}_R)$ . Exact solvers exist for the Riemann Problem for various sets of governing equations, such as the Euler equations [44], the equations of non-linear elasticity [5], or the shallow water equations [2], among others. There also exist approximate solvers for general conservative

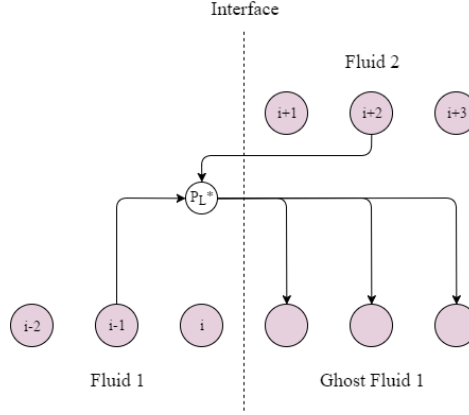


Figure 4: The Riemann Ghost Fluid Method

[31, 25] or non-conservative [11] hyperbolic systems of PDEs. The references given here form a very small sample of the work that has been done in this area.

The solution of the Riemann Problem usually takes the form of a set of waves, between which  $\mathbf{P}$  is constant. The waves can either be a contact discontinuity (across which pressure and velocity are continuous), a shock (across which all variables may be discontinuous), or a rarefaction (along which the variables vary continuously between their values on either side of the wave). The number and form of the waves are determined by the governing equations and the initial conditions. The states of the variables either side of the contact discontinuity in the middle are known as the *star states*. This qualitative description is depicted in Figure 3 on page 7.

Liu et al. [24] demonstrated that the original GFM fails to resolve strong shocks at material interfaces. This is because the method effectively solves two separate single-fluid Riemann problems. The waves present in these Riemann problems do not necessarily correspond to those in the real Riemann problem across the interface. The Riemann Ghost Fluid Method of Sambasivan et al. [40] aims to rectify this.

Given  $\mathbf{P}^n$  and  $x_n \in [(i + \frac{1}{2}) \Delta x, (i + \frac{3}{2}) \Delta x]$ , the ghost cells for fluid 1 are populated with the left star state of  $RP(\mathbf{P}_{i-1}^n, \mathbf{P}_{i+2}^n)$ , and the ghost cells for fluid 2 are populated with the right star state.  $RP(\mathbf{P}_{i-1}^n, \mathbf{P}_{i+2}^n)$  is solved rather than  $RP(\mathbf{P}_i^n, \mathbf{P}_{i+1}^n)$ , as  $\mathbf{P}_i^n, \mathbf{P}_{i+1}^n$  often contain errors generated by the fact that they lie on the material interface.  $\mathbf{P}^{n+1}$  is then generated as before from the newly formed  $\mathbf{P}^{(1)}, \mathbf{P}^{(2)}$ . This process is demonstrated in Figure 4 on page 8.

## 2. A Riemann Ghost Fluid Method for the GPR Model

### 2.1. Eigenstructure of the GPR Model

#### 2.1.1. Eigenvalues

Considering the primitive system matrix (90), it is clear that the eigenvalues of the GPR system in the first spatial axis consist of  $v_1$  repeated 8 times, along with the roots of:

$$\begin{vmatrix} (v_1 - \lambda) I & \Xi_2 \\ \Xi_1 & (v_1 - \lambda) I \end{vmatrix} = 0 \quad (22)$$

where



$$\Xi_1 = \begin{pmatrix} -\frac{1}{\rho} \frac{\partial \sigma_{11}}{\partial \rho} & \frac{1}{\rho} & -\frac{1}{\rho} \frac{\partial \sigma_{11}}{\partial A_{11}} & -\frac{1}{\rho} \frac{\partial \sigma_{11}}{\partial A_{21}} & -\frac{1}{\rho} \frac{\partial \sigma_{11}}{\partial A_{31}} \\ -\frac{1}{\rho} \frac{\partial \sigma_{21}}{\partial \rho} & 0 & -\frac{1}{\rho} \frac{\partial \sigma_{21}}{\partial A_{11}} & -\frac{1}{\rho} \frac{\partial \sigma_{21}}{\partial A_{21}} & -\frac{1}{\rho} \frac{\partial \sigma_{21}}{\partial A_{31}} \\ -\frac{1}{\rho} \frac{\partial \sigma_{31}}{\partial \rho} & 0 & -\frac{1}{\rho} \frac{\partial \sigma_{31}}{\partial A_{11}} & -\frac{1}{\rho} \frac{\partial \sigma_{31}}{\partial A_{21}} & -\frac{1}{\rho} \frac{\partial \sigma_{31}}{\partial A_{31}} \\ \frac{T_p}{\rho} & \frac{T_p}{\rho} & 0 & 0 & 0 \end{pmatrix} \quad (23)$$

$$\Xi_2 = \begin{pmatrix} \rho & 0 & 0 & 0 \\ \left(\rho c_0^2 + \sigma_{11} - \rho \frac{\partial \sigma_{11}}{\partial \rho}\right) & \left(\sigma_{21} - \rho \frac{\partial \sigma_{21}}{\partial \rho}\right) & \left(\sigma_{31} - \rho \frac{\partial \sigma_{31}}{\partial \rho}\right) & \frac{\rho c_h^2}{T_p} \\ A_{11} & A_{12} & A_{13} & 0 \\ A_{21} & A_{22} & A_{23} & 0 \\ A_{31} & A_{32} & A_{33} & 0 \end{pmatrix} \quad (24)$$

By the properties of block matrices<sup>2</sup>, the remaining eigenvalues are  $v_1$  and the roots of  $\left| (v_1 - \lambda)^2 I - \Xi_1 \Xi_2 \right| = 0$ . Thus,  $\lambda_i = v_1 \pm \sqrt{\tilde{\lambda}_i}$  where the  $\tilde{\lambda}_i$  are the eigenvalues of the following matrix:

$$\Xi = \Xi_1 \Xi_2 = \begin{pmatrix} \Omega_{11}^1 + \left(c_0^2 + \frac{\sigma_{11}}{\rho} - \frac{\partial \sigma_{11}}{\partial \rho}\right) & \Omega_{12}^1 + \left(\frac{\sigma_{21}}{\rho} - \frac{\partial \sigma_{21}}{\partial \rho}\right) & \Omega_{13}^1 + \left(\frac{\sigma_{31}}{\rho} - \frac{\partial \sigma_{31}}{\partial \rho}\right) & \frac{c_h^2}{T_p} \\ \Omega_{21}^1 & \Omega_{22}^1 & \Omega_{23}^1 & 0 \\ \Omega_{31}^1 & \Omega_{32}^1 & \Omega_{33}^1 & 0 \\ T_p + T_p \left(c_0^2 + \frac{\sigma_{11}}{\rho} - \frac{\partial \sigma_{11}}{\partial \rho}\right) & T_p \left(\frac{\sigma_{21}}{\rho} - \frac{\partial \sigma_{21}}{\partial \rho}\right) & T_p \left(\frac{\sigma_{31}}{\rho} - \frac{\partial \sigma_{31}}{\partial \rho}\right) & c_h^2 \end{pmatrix} \quad (25)$$

where  $\Omega$  is given shortly. Similar results hold for the other two spatial directions. In general it is not possible to express the eigenvalues of  $\Xi$  in terms of the eigenvalues of its submatrices. Note, however, that if  $c_t = 0$  then one of the eigenvalues is 0 and the remaining eigenvalues can be found analytically, using the form given in the appendix of [12].

It is straightforward to verify the following:

$$\frac{\partial \sigma_{ij}}{\partial A_{mn}} = -c_s^2 \rho \begin{pmatrix} \delta_{in} (A \operatorname{dev} (G))_{mj} + \delta_{jn} (A \operatorname{dev} (G))_{mi} \\ + A_{mi} G_{jn} + A_{mj} G_{in} - \frac{2}{3} G_{ij} A_{mn} \end{pmatrix} \quad (26)$$

The quantity  $\Omega$  is named here the *acoustic tensor*, due to its similarity to the acoustic tensor described in [6]:

$$\begin{aligned} \Omega_{ij}^d &= -\frac{1}{\rho} \frac{\partial \sigma_{id}}{\partial A_{kd}} A_{kj} - \frac{\sigma_{id}}{\rho} \delta_{dj} \\ &= c_s^2 \begin{pmatrix} \delta_{id} (G \operatorname{dev} (G))_{dj} + (G \operatorname{dev} (G))_{id} \delta_{dj} \\ + (G \operatorname{dev} (G))_{ij} + G_{ij} G_{dd} + \frac{1}{3} G_{dj} G_{id} \end{pmatrix} \\ &= c_s^2 \left( E^d G \operatorname{dev} (G) + G \operatorname{dev} (G) E^d + G \operatorname{dev} (G) + G_{dd} G + \frac{1}{3} G_d G_d^T \right) \end{aligned} \quad (27)$$

where  $E_{ij}^d = \delta_{id} \delta_{jd}$ .

### 2.1.2. Eigenvectors

The following results are presented for an unmixed material ( $z \equiv 0$ ).

---

<sup>2</sup>If  $A$  is invertible,  $\det \begin{pmatrix} A & B \\ C & D \end{pmatrix} = \det(A) \det(D - CA^{-1}B)$

*With Heat Conduction.* By hyperbolicity of the system,  $\Xi$  can be expressed as:

$$\Xi = Q^{-1}D^2Q \quad (28)$$

where  $D$  is a diagonal matrix with positive diagonal entries. The eigenvectors corresponding to  $\lambda_i = v_1 \pm \sqrt{\tilde{\lambda}_i}$  take the form  $\begin{pmatrix} \hat{u} & 0_6 & \tilde{u} & 0_2 \end{pmatrix}^T$  where  $\hat{u} \in \mathbb{R}^5, \tilde{u} \in \mathbb{R}^4$  satisfy:

$$\begin{pmatrix} v_1 I & \Xi_2 \\ \Xi_1 & v_1 I \end{pmatrix} \begin{pmatrix} \hat{u} \\ \tilde{u} \end{pmatrix} = \begin{pmatrix} v_1 \pm \sqrt{\tilde{\lambda}_i} \end{pmatrix} \begin{pmatrix} \hat{u} \\ \tilde{u} \end{pmatrix} \quad (29)$$

Thus,  $\Xi_2 \tilde{u} = \pm \sqrt{\tilde{\lambda}_i} \hat{u}$  and  $\Xi_1 \hat{u} = \pm \sqrt{\tilde{\lambda}_i} \tilde{u}$ . Combining these results,  $\Xi \tilde{u} = \tilde{\lambda}_i \tilde{u}$ . Thus,  $\tilde{u}$  is a right eigenvector of  $\Xi$  and, taking the form  $Q^{-1}e_i$  for some  $i = 1 \dots 4$ .

The four eigenvectors corresponding to eigenvalues of the form  $v_1 + \sqrt{\tilde{\lambda}_i}$  are columns 1-4 of matrix  $R$  in (30). Those corresponding to eigenvalues of the form  $v_1 - \sqrt{\tilde{\lambda}_i}$  are columns 5-8. By inspection, it can be verified that the remaining 9 eigenvectors (corresponding to eigenvalue  $v_1$ ) are the remaining columns.

A similar analysis yields the left eigenvectors as the rows of (32).

$$R = \left\{ \begin{pmatrix} \frac{1}{2}\Xi_2 (D^2Q)^{-1} & \frac{1}{2}\Xi_2 (D^2Q)^{-1} \\ 0_{6,4} & 0_{6,4} \\ \frac{1}{2}(DQ)^{-1} & -\frac{1}{2}(DQ)^{-1} \\ 0_{2,4} & 0_{2,4} \end{pmatrix}, \begin{pmatrix} -cT_p \\ cT_\rho \\ c\Pi_d^{-1}w \\ 0_{12,1} \end{pmatrix}, \begin{pmatrix} 0_{2,3} & 0_{2,3} \\ -\Pi_1^{-1}\Pi_2 & -\Pi_1^{-1}\Pi_3 \\ I_3 & 0_{3,3} \\ 0_{3,3} & I_3 \\ 0_{6,3} & 0_{6,3} \end{pmatrix}, \begin{pmatrix} 0_{15,2} \\ I_2 \end{pmatrix} \right\} \quad (30)$$

where

$$w = T_p \frac{\partial \sigma_d}{\partial \rho} + T_\rho e_d \quad (31a)$$

$$c = \frac{1}{e_d^T (\Pi_d A)^{-1} w + \frac{T_p}{\rho}} \quad (31b)$$

$$L = \left\{ \begin{pmatrix} Q\Xi_1 & -\frac{1}{\rho}Q_{:,1:3}\Pi_2 & -\frac{1}{\rho}Q_{:,1:3}\Pi_3 & DQ & 0_{4,2} \\ Q\Xi_1 & -\frac{1}{\rho}Q_{:,1:3}\Pi_2 & -\frac{1}{\rho}Q_{:,1:3}\Pi_3 & -DQ & 0_{4,2} \\ -\frac{1}{\rho} & 0 & e_d^T A^{-1} & e_d^T A^{-1} \Pi_1^{-1} \Pi_2 & e_d^T A^{-1} \Pi_1^{-1} \Pi_3 & 0_{1,6} \end{pmatrix}, \begin{pmatrix} 0_{3,5} & I_3 & 0_{3,3} & 0_{3,6} \\ 0_{3,5} & 0_{3,3} & I_3 & 0_{3,6} \\ 0_{2,15} & I_2 \end{pmatrix} \right\} \quad (32)$$

*Without Heat Conduction.* If the system does not include the heat conduction terms, the eigenstructure of the system matrix changes.  $\Xi_1, \Xi_2, \Xi$  now take the following values:

$$\Xi_1 = \begin{pmatrix} -\frac{1}{\rho} \frac{\partial \sigma_{11}}{\partial \rho} & \frac{1}{\rho} & -\frac{1}{\rho} \frac{\partial \sigma_{11}}{\partial A_{11}} & -\frac{1}{\rho} \frac{\partial \sigma_{11}}{\partial A_{21}} & -\frac{1}{\rho} \frac{\partial \sigma_{11}}{\partial A_{31}} \\ -\frac{1}{\rho} \frac{\partial \sigma_{21}}{\partial \rho} & 0 & -\frac{1}{\rho} \frac{\partial \sigma_{21}}{\partial A_{11}} & -\frac{1}{\rho} \frac{\partial \sigma_{21}}{\partial A_{21}} & -\frac{1}{\rho} \frac{\partial \sigma_{21}}{\partial A_{31}} \\ \frac{\partial \rho}{\partial \rho} & 0 & \frac{\partial A_{11}}{\partial A_{11}} & \frac{\partial A_{21}}{\partial A_{21}} & \frac{\partial A_{31}}{\partial A_{31}} \\ -\frac{1}{\rho} \frac{\partial \sigma_{31}}{\partial \rho} & 0 & -\frac{1}{\rho} \frac{\partial \sigma_{31}}{\partial A_{11}} & -\frac{1}{\rho} \frac{\partial \sigma_{31}}{\partial A_{21}} & -\frac{1}{\rho} \frac{\partial \sigma_{31}}{\partial A_{31}} \end{pmatrix} \quad (33)$$

$$\Xi_2 = \begin{pmatrix} \rho & 0 & 0 \\ \left(\rho c_0^2 + \sigma_{11} - \rho \frac{\partial \sigma_{11}}{\partial \rho}\right) & \left(\sigma_{21} - \rho \frac{\partial \sigma_{21}}{\partial \rho}\right) & \left(\sigma_{31} - \rho \frac{\partial \sigma_{31}}{\partial \rho}\right) \\ A_{11} & A_{12} & A_{13} \\ A_{21} & A_{22} & A_{23} \\ A_{31} & A_{32} & A_{33} \end{pmatrix} \quad (34)$$

$$\Xi = \Xi_1 \Xi_2 = \begin{pmatrix} \Omega_{11}^1 + \left(c_0^2 + \frac{\sigma_{11}}{\rho} - \frac{\partial \sigma_{11}}{\partial \rho}\right) & \Omega_{12}^1 + \left(\frac{\sigma_{21}}{\rho} - \frac{\partial \sigma_{21}}{\partial \rho}\right) & \Omega_{13}^1 + \left(\frac{\sigma_{31}}{\rho} - \frac{\partial \sigma_{31}}{\partial \rho}\right) \\ \Omega_{21}^1 & \Omega_{22}^1 & \Omega_{23}^1 \\ \Omega_{31}^1 & \Omega_{32}^1 & \Omega_{33}^1 \end{pmatrix} \quad (35)$$

Using the eigendecomposition  $\Xi = Q^{-1} D^2 Q$  as before, we have:

$$R = \left\{ \begin{pmatrix} \frac{1}{2} \Xi_2 (D^2 Q)^{-1} & \frac{1}{2} \Xi_2 (D^2 Q)^{-1} \\ 0_{6,3} & 0_{6,3} \\ \frac{1}{2} (DQ)^{-1} & -\frac{1}{2} (DQ)^{-1} \end{pmatrix}, \begin{pmatrix} 1 & 0 \\ 0 & 1 \\ -\Pi_1^{-1} \frac{\partial \sigma_1}{\partial \rho} & \Pi_1^{-1} \mathbf{e}_1 \\ \mathbf{0}_9 & \mathbf{0}_9 \end{pmatrix}, \begin{pmatrix} 0_{2,3} & 0_{2,3} \\ -\Pi_1^{-1} \Pi_2 & -\Pi_1^{-1} \Pi_3 \\ I_3 & 0_{3,3} \\ 0_{3,3} & I_3 \\ 0_{3,3} & 0_{3,3} \end{pmatrix} \right\} \quad (36)$$

By considering their products with the first 8 columns of  $R$ , two of the left eigenvectors corresponding the the 7th and 8th right eigenvectors must come in the form of the rows of the following matrix:

$$\begin{pmatrix} W & X & Y & Z \end{pmatrix} \quad (37)$$

where  $W \in \mathbb{R}^{2,5}$  and  $X, Y, Z \in \mathbb{R}^{2,3}$ , and:

$$W \Xi_2 (D^2 Q)^{-1} + Z (DQ)^{-1} = 0 \quad (38a)$$

$$W \Xi_2 (D^2 Q)^{-1} - Z (DQ)^{-1} = 0 \quad (38b)$$

$$W \begin{pmatrix} 0_{2,3} \\ -\Pi_1^{-1} \Pi_2 \end{pmatrix} + X = 0 \quad (38c)$$

$$W \begin{pmatrix} 0_{2,3} \\ -\Pi_1^{-1} \Pi_3 \end{pmatrix} + Y = 0 \quad (38d)$$

Thus:

$$Z = 0 \quad (39a)$$

$$X = W_{:,3:5} \Pi_1^{-1} \Pi_2 \quad (39b)$$

$$Y = W_{:,3:5} \Pi_1^{-1} \Pi_3 \quad (39c)$$

and

$$W \begin{pmatrix} \rho & 0 & 0 & 1 & 0 \\ \left(\rho c_0^2 + \sigma_{11} - \rho \frac{\partial \sigma_{11}}{\partial \rho}\right) & \left(\sigma_{21} - \rho \frac{\partial \sigma_{21}}{\partial \rho}\right) & \left(\sigma_{31} - \rho \frac{\partial \sigma_{31}}{\partial \rho}\right) & 0 & 1 \\ A_{11} & A_{12} & A_{13} & \vdots & \vdots \\ A_{21} & A_{22} & A_{23} & -\Pi_1^{-1} \frac{\partial \sigma_1}{\partial \rho} & \Pi_1^{-1} \mathbf{e}_1 \\ A_{31} & A_{32} & A_{33} & \vdots & \vdots \end{pmatrix} = WM = \begin{pmatrix} 0 & 0 & 0 & 1 & 0 \\ 0 & 0 & 0 & 0 & 1 \end{pmatrix} \quad (40)$$

By the properties of block matrices:

$$M^{-1} = \begin{pmatrix} -A^{-1}C(I - BA^{-1}C)^{-1} & A^{-1}(I + C(I - BA^{-1}C)^{-1}BA^{-1}) \\ (I - BA^{-1}C)^{-1} & -(I - BA^{-1}C)^{-1}BA^{-1} \end{pmatrix} \quad (41)$$

where

$$B = \begin{pmatrix} \rho & 0 & 0 \\ \left(\rho c_0^2 + \sigma_{11} - \rho \frac{\partial \sigma_{11}}{\partial \rho}\right) & \left(\sigma_{21} - \rho \frac{\partial \sigma_{21}}{\partial \rho}\right) & \left(\sigma_{31} - \rho \frac{\partial \sigma_{31}}{\partial \rho}\right) \end{pmatrix} \quad (42a)$$

$$C = \begin{pmatrix} \cdots & -\Pi_1^{-1} \frac{\partial \sigma_1}{\partial \rho} & \cdots \\ \cdots & \Pi_1^{-1} \mathbf{e}_1 & \cdots \end{pmatrix}^T \quad (42b)$$

Thus:

$$W = \begin{pmatrix} (I - BA^{-1}C)^{-1} & -(I - BA^{-1}C)^{-1}BA^{-1} \end{pmatrix} \quad (43)$$

$$W = (I - BA^{-1}C)^{-1} \begin{pmatrix} I_2 & -BA^{-1} \end{pmatrix} \quad (44a)$$

$$X = -(I - BA^{-1}C)^{-1}BA^{-1}\Pi_1^{-1}\Pi_2 \quad (44b)$$

$$Y = -(I - BA^{-1}C)^{-1}BA^{-1}\Pi_1^{-1}\Pi_3 \quad (44c)$$

$$L = \left\{ \begin{pmatrix} Q\Xi_1 & -\frac{1}{\rho}Q\Pi_2 & -\frac{1}{\rho}Q\Pi_3 & DQ \\ Q\Xi_1 & -\frac{1}{\rho}Q\Pi_2 & -\frac{1}{\rho}Q\Pi_3 & -DQ \end{pmatrix} \right. \\ \left. (I_2 - BA^{-1}C)^{-1} \begin{pmatrix} I_2 & -BA^{-1} & -BA^{-1}\Pi_1^{-1}\Pi_2 & -BA^{-1}\Pi_1^{-1}\Pi_3 & 0_{2,3} \end{pmatrix} \begin{pmatrix} 0_{3,5} & I_3 & 0_{3,3} & 0_{3,3} \\ 0_{3,5} & 0_{3,3} & I_3 & 0_{3,3} \end{pmatrix} \right\} \quad (45)$$

## 2.2. A GPR Riemann Ghost Fluid Method

### 2.3. Solving the Riemann Problem

Barton et al. have presented an RGFM for the equations of non-linear elasticity [7, 4]. Owing to the similarity of the structure of the non-linear elasticity equations to those of the GPR model (differing only in the presence of source terms, the form of the shear stress tensor, and possibly the EOS), their method is built upon here. The resulting method is named the *GPR-RGFM*.

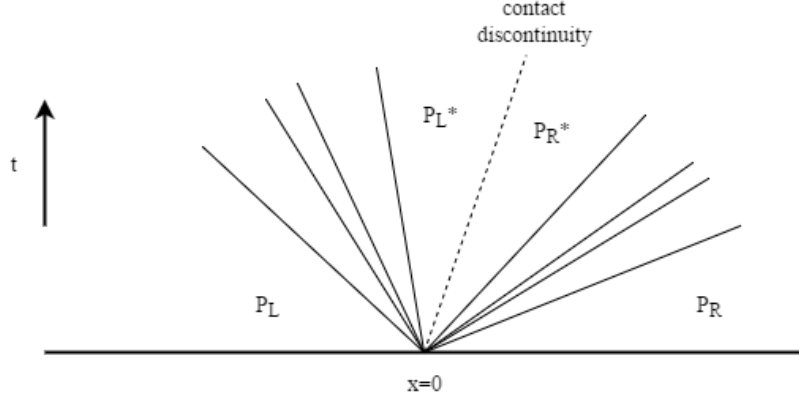


Figure 5: The Riemann Problem for the GPR model, assuming all waves are distinct

The Riemann Problem of the GPR model takes the form demonstrated in Figure 5 on page 13. Assuming all waves are distinct, there are four waves on either side of the contact discontinuity. On each side, one wave corresponds to the thermal impulse (manifesting as a heat wave) and the other three correspond to the distortion components in the axis in which the Riemann Problem is considered (manifesting as two shear waves and one longitudinal pressure wave). It is important to note that - owing to the source terms - the star states are not constant in the spacetime region in which they reside, so the method presented here produces only an approximation to them.

The method is presented here along the first spatial axis. It can easily be adapted along any axis by taking the components of all relevant vector quantities (velocity, distortion, and thermal impulse) in the direction normal to the interface.

Denote the vector of primitive variables by  $\mathbf{P}$ . Take the set of left eigenvectors  $L$  (??) with eigenvalues  $\{\lambda_i\}$ . We have the standard set of relations along characteristics (curves along which  $\frac{dx}{dt} = \lambda_i$ ):<sup>3</sup>

$$L \cdot d\mathbf{P} = dt \cdot L \cdot \mathbf{S} \quad (46)$$

In what follows, we enact an operator splitting of the two processes present in the system (46):

$$L \cdot d\mathbf{P} = \mathbf{0} \quad (47a)$$

$$\frac{d\mathbf{P}}{dt} = \mathbf{S} \quad (47b)$$

$\mathbf{P}^{*K}$  is now sought, where  $K = L$  or  $K = R$ , denoting the left or right sides of the interface, respectively. Take the following linearization:

<sup>3</sup>Take the hyperbolic system  $\frac{\partial \mathbf{P}}{\partial t} + M \frac{\partial \mathbf{P}}{\partial x} = \mathbf{S}$ . Let  $\mathbf{l}_i^T M = \lambda_i \mathbf{l}_i^T$ . Along characteristics corresponding to  $\lambda_i$ :

$$\begin{aligned} \mathbf{l}_i^T \left( \frac{\partial \mathbf{P}}{\partial t} + M \frac{\partial \mathbf{P}}{\partial x} \right) &= \mathbf{l}_i^T \left( \frac{\partial \mathbf{P}}{\partial t} + \frac{dx}{dt} \frac{\partial \mathbf{P}}{\partial x} \right) \\ &= \mathbf{l}_i^T \frac{d\mathbf{P}}{dt} = \mathbf{l}_i^T \mathbf{S} \end{aligned}$$

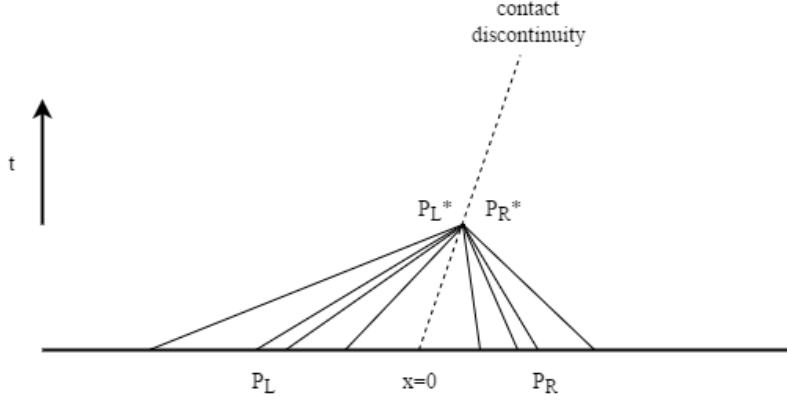


Figure 6: Different sets of characteristic curves, traveling from their respective initial points to the star region

$$d\mathbf{P}^K \approx \mathbf{P}^{*K} - \mathbf{P}^K \quad (48)$$

13 relations from (47a) are taken: four regarding the 4 sets of characteristics traveling into the contact discontinuity from side  $K$  (with speeds greater or less than  $v$  for  $K = L$  or  $K = R$ , respectively), and nine relating to the contact discontinuity itself. This is demonstrated in Figure 6 on page 14. Four more relations must be derived to solve the system for  $\mathbf{P}^{*K}$ . Expanding the Taylor series of  $\Sigma^*, T^*$ :

$$\Sigma^* = \Sigma + (\rho^* - \rho) \frac{\partial \Sigma}{\partial \rho} + (p^* - p) \frac{\partial \Sigma}{\partial p} + (A_{mn}^* - A_{mn}) \frac{\partial \Sigma}{\partial A_{mn}} + O(d\mathbf{P}^2) \quad (49a)$$

$$T^* = T + (\rho^* - \rho) \frac{\partial T}{\partial \rho} + (p^* - p) \frac{\partial T}{\partial p} + O(d\mathbf{P}^2) \quad (49b)$$

Thus, we have:

$$\Sigma^* - \Sigma \approx (p^* - p) I - (\rho^* - \rho) \frac{\partial \sigma}{\partial \rho} - (A_{mn}^* - A_{mn}) \frac{\partial \sigma}{\partial A_{mn}} \quad (50a)$$

$$T^* - T \approx (\rho^* - \rho) \frac{\partial T}{\partial \rho} + (p^* - p) \frac{\partial T}{\partial p} \quad (50b)$$

These are the extra required relations. Thus we have:

$$\hat{L}^K \cdot (\mathbf{P}^{*K} - \mathbf{P}^K) = \mathbf{c}^K \quad (51)$$

where  $\hat{L}^K$  takes the form found in (66), with  $\xi = -1$  for  $K = R$  and  $\xi = 1$  for  $K = L$ , and:

$$\mathbf{c}^K = \begin{pmatrix} \Sigma_1^{*K} - \Sigma_1^K \\ T^{*K} - T^K \\ 0 \end{pmatrix} \quad (52)$$

The inverse of  $\hat{L}^K$  takes the form found in (67).

$\hat{L}^K, \hat{L}^{K-1}$  are evaluated at  $\mathbf{P}^K$ . It remains to find expressions for  $\Sigma^*$  and  $T^*$  in terms of  $\mathbf{P}^L, \mathbf{P}^R$  to close the system. The obtained values depend on the boundary conditions chosen, as explained below.

### 2.3.1. Stick Boundary Conditions

The following boundary conditions are used:

$$\Sigma_1^{*L} = \Sigma_1^{*R} \quad (53a)$$

$$T^{*L} = T^{*R} \quad (53b)$$

$$\mathbf{v}^{*L} = \mathbf{v}^{*R} \quad (53c)$$

$$q_1^{*L} = q_1^{*R} \quad (53d)$$

Taking the relevant rows of  $\mathbf{P}^{*K} = \mathbf{P}^K + \hat{L}^{K-1} \mathbf{c}^K$ :

$$\begin{pmatrix} v^* \\ J_1^* \end{pmatrix} = \begin{pmatrix} v^K \\ J_1^K \end{pmatrix} + Y^K \left( \begin{pmatrix} \Sigma_1^* \\ T^* \end{pmatrix} - \begin{pmatrix} \Sigma_1^K \\ T^K \end{pmatrix} \right) \quad (54)$$

Thus:

$$\begin{pmatrix} \Sigma_1^* \\ T^* \end{pmatrix} = (Y^L - Y^R)^{-1} \left( \begin{pmatrix} v^R \\ J_1^R \end{pmatrix} - \begin{pmatrix} v^L \\ J_1^L \end{pmatrix} + Y^L \begin{pmatrix} \Sigma_1^L \\ T^L \end{pmatrix} - Y^R \begin{pmatrix} \Sigma_1^R \\ T^R \end{pmatrix} \right) \quad (55)$$

### 2.3.2. Slip Boundary Conditions

The following boundary conditions are used:

$$\Sigma_{11}^{*L} = \Sigma_{11}^{*R} \quad (56a)$$

$$\Sigma_{12}^{*L}, \Sigma_{12}^{*R} = 0 \quad (56b)$$

$$\Sigma_{13}^{*L}, \Sigma_{13}^{*R} = 0 \quad (56c)$$

$$T^{*L} = T^{*R} \quad (56d)$$

$$v_1^{*L} = v_1^{*R} \quad (56e)$$

$$q_1^{*L} = q_1^{*R} \quad (56f)$$

Taking the relevant rows of  $\mathbf{P}^{*K} = \mathbf{P}^K + \hat{L}^{K-1} \mathbf{c}^K$ :

$$\begin{pmatrix} v_1^* \\ J_1^* \end{pmatrix} = \begin{pmatrix} v_1^K \\ J_1^K \end{pmatrix} + \tilde{Y}^K \left( \begin{pmatrix} \Sigma_{11}^* \\ 0 \\ 0 \\ T^* \end{pmatrix} - \begin{pmatrix} \Sigma_{11}^K \\ \Sigma_{12}^K \\ \Sigma_{13}^K \\ T^K \end{pmatrix} \right) \quad (57)$$

where

$$\tilde{Y}^K = \begin{pmatrix} \mathbf{Y}_1^K \\ \mathbf{Y}_4^K \end{pmatrix} \quad (58)$$

Thus:

$$\begin{pmatrix} \Sigma_{11}^* \\ T^* \end{pmatrix} = (\hat{Y}^L - \hat{Y}^R)^{-1} \left( \begin{pmatrix} v_1^R \\ J_1^R \end{pmatrix} - \begin{pmatrix} v_1^K \\ J_1^K \end{pmatrix} + Y^L \begin{pmatrix} \Sigma_1^L \\ T^L \end{pmatrix} - Y^R \begin{pmatrix} \Sigma_1^R \\ T^R \end{pmatrix} \right) \quad (59)$$

where

$$\hat{Y}^K = \begin{pmatrix} Y_{11}^K & Y_{14}^K \\ Y_{41}^K & Y_{44}^K \end{pmatrix} \quad (60)$$

### 2.3.3. Vacuum Boundary Conditions

The following boundary conditions are used:

$$\Sigma_1^* = \mathbf{0} \quad (61a)$$

$$q_1^* = 0 \quad (61b)$$

Taking the relevant row of  $\mathbf{P}^{*K} = \mathbf{P}^K + \hat{L}^{K-1} \mathbf{c}^K$ :

$$J_1^* = J_1^K + \mathbf{Y}_4^K \cdot \left( \begin{pmatrix} \mathbf{0} \\ T^* \end{pmatrix} - \begin{pmatrix} \Sigma_1^K \\ T^K \end{pmatrix} \right) \quad (62)$$

As  $q_1^* = 0$  implies that  $J_1^* = 0$ , we have:

$$T^* = \frac{1}{Y_{44}^K} \left( \mathbf{Y}_4^K \cdot \begin{pmatrix} \Sigma_1^K \\ T^K \end{pmatrix} - J_1^K \right) = T^K + \frac{\mathbf{Y}_{4,:3}^K \cdot \Sigma_1^K - J_1^K}{Y_{44}^K} \quad (63)$$

### 2.3.4. Iteration

(51) is solved for  $\mathbf{P}^{*K}$ , which is taken to be the star state if the following conditions are satisfied:

$$\frac{|\Sigma_1^{*L} - \Sigma_1^{*R}|}{\min(\rho_0^L, \rho_0^R) \times \min(c_s^L, c_s^R)^2} < TOL \quad (64a)$$

$$\frac{|v_1^L - v_1^R|}{\min(c_s^L, c_s^R)} < TOL \quad (64b)$$

$$\frac{|q_1^L - q_1^R|}{\min(\tilde{q}^L, \tilde{q}^R)} < TOL \quad (64c)$$

$$\frac{|T^L - T^R|}{\min(T_0^L, T_0^R)} < TOL \quad (64d)$$

where

$$\tilde{q} = \frac{c_t^2}{\rho_0} \sqrt{\frac{T_0^3}{c_V}} \quad (65)$$

These convergence criteria are chosen so that the variables required to be less than  $TOL$  are dimensionless. At every iteration, (47b) is solved using the ODE solvers described in ??.



## 2.4. Linear Conditions

Replacing the first four lines of (??) with the conditions

$$\hat{L}^K = \left\{ \begin{pmatrix} -\frac{\partial \sigma_d}{\partial \rho} & \mathbf{e}_d & -\Pi_1 & -\Pi_2 & -\Pi_3 & 0_{3,6} \\ \frac{\partial T}{\partial \rho} & \frac{\partial T}{\partial p} & 0_{1,3} & 0_{1,3} & 0_{1,3} & 0_{1,6} \\ Q\Xi_1 & -\frac{1}{\rho}Q_{:,1:3}\Pi_2 & -\frac{1}{\rho}Q_{:,1:3}\Pi_3 & \xi DQ & 0_{4,2} \\ -\frac{1}{\rho} & 0 & \mathbf{e}_d^T A^{-1} & \mathbf{e}_d^T A^{-1}\Pi_1^{-1}\Pi_2 & \mathbf{e}_d^T A^{-1}\Pi_1^{-1}\Pi_3 & 0_{1,6} \end{pmatrix} \right. \\ \left. \begin{pmatrix} 0_{3,5} & I_3 & 0_{3,3} & 0_{3,6} \\ 0_{3,5} & 0_{3,3} & I_3 & 0_{3,6} \\ 0_{2,15} & I_2 \end{pmatrix} \right\} \quad (66)$$

$$\hat{L}^{K-1} = \left\{ \begin{pmatrix} X \\ 0_{6,4} \\ Y \\ 0_{2,4} \end{pmatrix}, \begin{pmatrix} 0_{11,4} \\ \xi (DQ)^{-1} \\ 0_{2,4} \end{pmatrix}, \begin{pmatrix} -cT_p \\ cT_\rho \\ c\Pi_d^{-1}\mathbf{w} \\ 0_{12,1} \end{pmatrix}, \begin{pmatrix} 0_{2,3} & 0_{2,3} \\ -\Pi_1^{-1}\Pi_2 & -\Pi_1^{-1}\Pi_3 \\ I_3 & 0_{3,3} \\ 0_{3,3} & I_3 \\ 0_{6,3} & 0_{6,3} \end{pmatrix}, \begin{pmatrix} 0_{15,2} \\ I_2 \end{pmatrix} \right\} \quad (67)$$

where:

$$X = \begin{pmatrix} \vdots & \vdots & \ddots & \vdots & \ddots \\ -\frac{\partial \sigma_d}{\partial \rho} & \mathbf{e}_d & \cdots & -\Pi_1 & \cdots \\ \vdots & \vdots & \ddots & \vdots & \ddots \\ \frac{\partial T}{\partial \rho} & \frac{\partial T}{\partial p} & 0 & 0 & 0 \\ -\frac{1}{\rho} & 0 & \cdots & \mathbf{e}_d^T A^{-1} & \cdots \end{pmatrix}^{-1} \begin{pmatrix} 1 & 0 & 0 & 0 \\ 0 & 1 & 0 & 0 \\ 0 & 0 & 1 & 0 \\ 0 & 0 & 0 & 1 \\ 0 & 0 & 0 & 0 \end{pmatrix} \quad (68a)$$

$$Y = -\xi Q^{-1} D^{-1} Q \Xi_1 X \quad (68b)$$

By inversion of block matrices<sup>4</sup>:

$$\begin{pmatrix} \vdots & \vdots & \ddots & \vdots & \ddots \\ -\frac{\partial \sigma_d}{\partial \rho} & \mathbf{e}_d & \cdots & -\Pi_1 & \cdots \\ \vdots & \vdots & \ddots & \vdots & \ddots \\ \frac{\partial T}{\partial \rho} & \frac{\partial T}{\partial p} & 0 & 0 & 0 \\ -\frac{1}{\rho} & 0 & \cdots & \mathbf{e}_d^T A^{-1} & \cdots \end{pmatrix}^{-1} = \begin{pmatrix} D^{-1} C Z^{-1} & D^{-1} (I - C Z^{-1} B D^{-1}) \\ -Z^{-1} & Z^{-1} B D^{-1} \end{pmatrix} \quad (69)$$

where

$$\begin{cases} B = \begin{pmatrix} \vdots & \vdots \\ -\frac{\partial \sigma_d}{\partial \rho} & \mathbf{e}_d \\ \vdots & \vdots \end{pmatrix} & C = \begin{pmatrix} 0 & 0 & 0 \\ \cdots & \mathbf{e}_d^T A^{-1} & \cdots \end{pmatrix} \\ D = \begin{pmatrix} \frac{\partial T}{\partial \rho} & \frac{\partial T}{\partial p} \\ -\frac{1}{\rho} & 0 \end{pmatrix} & Z = \Pi_1 + \frac{\rho}{T_p} \left( T_p \frac{\partial \sigma_d}{\partial \rho} + T_\rho \mathbf{e}_d \right) \mathbf{e}_d^T A^{-1} \end{cases} \quad (70)$$

---


$${}^4 \begin{pmatrix} A & B \\ C & D \end{pmatrix}^{-1} = \begin{pmatrix} (A - B D^{-1} C)^{-1} & -(A - B D^{-1} C)^{-1} B D^{-1} \\ -D^{-1} C (A - B D^{-1} C)^{-1} & D^{-1} (I + C (A - B D^{-1} C)^{-1} B D^{-1}) \end{pmatrix}$$

### 2.5. The Case without Heat Conduction

If the heat conduction terms are dropped from the GPR model, the eigenstructure of the system changes, along with the solution of the linear conditions.  $\Xi$  retains the same definition, but is now a  $3 \times 3$  matrix (comprising the top-left corner of  $\Xi$  under heat conduction). Thus,  $Q, D$  are also  $3 \times 3$  matrices. Taking the eigenvectors (45), the linear conditions become:

$$\hat{L}^K = \left\{ \begin{array}{c} \begin{pmatrix} -\frac{\partial \sigma_d}{\partial \rho} & \mathbf{e}_d & -\Pi_1 & -\Pi_2 & -\Pi_3 \\ Q\Xi_1 & -\frac{1}{\rho}Q\Pi_2 & -\frac{1}{\rho}Q\Pi_3 & \xi DQ \end{pmatrix} \\ (I - BA^{-1}C)^{-1} \begin{pmatrix} I_2 & -BA^{-1} & -BA^{-1}\Pi_1^{-1}\Pi_2 & -BA^{-1}\Pi_1^{-1}\Pi_3 & 0_{2,3} \end{pmatrix} \\ \begin{pmatrix} 0_{3,5} & I_3 & 0_{3,3} & 0_{3,3} \\ 0_{3,5} & 0_{3,3} & I_3 & 0_{3,3} \end{pmatrix} \end{array} \right\} \quad (71)$$

$$\hat{L}^{K-1} = \left\{ \begin{pmatrix} X \\ 0_{6,3} \\ Y \end{pmatrix}, \begin{pmatrix} 0_{11,3} \\ \xi(DQ)^{-1} \end{pmatrix}, \begin{pmatrix} 1 & 0 \\ 0 & 1 \\ -\Pi_1^{-1}\frac{\partial \sigma_1}{\partial \rho} & \Pi_1^{-1}\mathbf{e}_1 \\ \mathbf{0}_9 & \mathbf{0}_9 \end{pmatrix}, \begin{pmatrix} 0_{2,3} & 0_{2,3} \\ -\Pi_1^{-1}\Pi_2 & -\Pi_1^{-1}\Pi_3 \\ I_3 & 0_{3,3} \\ 0_{3,3} & I_3 \\ 0_{3,3} & 0_{3,3} \end{pmatrix} \right\} \quad (72)$$

where:

$$X = \begin{pmatrix} \vdots & \vdots & \ddots & \vdots & \ddots \\ -\frac{\partial \sigma_d}{\partial \rho} & \mathbf{e}_d & \cdots & -\Pi_1 & \cdots \\ \vdots & \vdots & \ddots & \vdots & \ddots \\ \vdots & \ddots & \ddots & \vdots & \ddots \\ (I - BA^{-1}C)^{-1} & \cdots & \cdots & -(I - BA^{-1}C)^{-1}BA^{-1} & \cdots \end{pmatrix}^{-1} \begin{pmatrix} 1 & 0 & 0 & 0 \\ 0 & 1 & 0 & 0 \\ 0 & 0 & 1 & 0 \\ 0 & 0 & 0 & 1 \\ 0 & 0 & 0 & 0 \end{pmatrix} \quad (73a)$$

$$Y = -\xi Q^{-1}D^{-1}Q\Xi_1 X \quad (73b)$$

By inversion of block matrices:

$$\begin{aligned} & \begin{pmatrix} \vdots & \vdots & \ddots & \vdots & \ddots \\ -\frac{\partial \sigma_d}{\partial \rho} & \mathbf{e}_d & \cdots & -\Pi_1 & \cdots \\ \vdots & \vdots & \ddots & \vdots & \ddots \\ \vdots & \ddots & \ddots & \vdots & \ddots \\ (I - BA^{-1}C)^{-1} & \cdots & \cdots & -(I - BA^{-1}C)^{-1}BA^{-1} & \cdots \end{pmatrix}^{-1} \\ &= \begin{pmatrix} -BA^{-1}Z & (I + BA^{-1}Z\tilde{B})(I - BA^{-1}\Pi_1^{-1}\tilde{B}) \\ -Z & Z\tilde{B}(I - BA^{-1}\Pi_1^{-1}\tilde{B}) \end{pmatrix} \end{aligned} \quad (74)$$

where

$$Z = \left( \Pi_1 - \tilde{B} B A^{-1} \right)^{-1} \quad (75a)$$

$$\tilde{B} = \begin{pmatrix} \cdots & -\frac{\partial \sigma_1}{\partial \rho} & \cdots \\ \cdots & \mathbf{e}_1 & \cdots \end{pmatrix}^T \quad (75b)$$

$$B = \begin{pmatrix} \rho & 0 & 0 \\ \left( \rho c_0^2 + \sigma_{11} - \rho \frac{\partial \sigma_{11}}{\partial \rho} \right) & \left( \sigma_{21} - \rho \frac{\partial \sigma_{21}}{\partial \rho} \right) & \left( \sigma_{31} - \rho \frac{\partial \sigma_{31}}{\partial \rho} \right) \end{pmatrix} \quad (75c)$$

### 3. Results

The GPR-RGFM is now assessed. The first five tests in this chapter are Riemann problems that have appeared elsewhere in the literature. Exact solutions to these problems have been calculated by various methods. The last test is new; it assess the ability of the GPR-RGFM to correctly model heat conduction across interfaces. The EOS parameters for three commonly-used fluids are given in Table 1 on page 19.

	$\rho_0$	$c_v$	$\gamma$	$p_\infty$	$b_0$	$c_\alpha$	$\mu$	$P_r$
Air	1.18	718	1.4	-	55	50	$1.85 \times 10^{-5}$	0.714
Helium	0.163	3127	5/3	-	55	50	$1.99 \times 10^{-5}$	0.688
Water	997	950	4.4	$6 \times 10^8$	1	1	$10^{-3}$	7

Table 1: EOS parameters for different fluids (using SI units)

#### 3.1. Helium Bubble

The interface between two different gases is now modeled. As in Test B of Wang et al. [45], a bubble of helium - surrounded by air - initially occupies the region  $x \in [0.4, 0.6]$ . A shock front in the air, initially at  $x = 0.05$ , travels towards the helium bubble. The initial conditions are given in Table 2 on page 19 and the EOS parameters for each material are given in Table 1 on page 19.

200 cells are used. Reference solutions are computed using the exact solver for mixed ideal gas Riemann problems under the Euler equations (presented in [43]). The results for times  $t = 7 \times 10^{-4}$  and  $t = 14 \times 10^{-4}$  are displayed in Figure 7 on page 20. In the former, the shock is about to hit the helium bubble (corresponding to the region of low density). In the latter, the shock has traveled through the helium bubble, compressing it slightly, and the bubble itself has moved almost 0.1 spatial units to the right. There is good correspondence with the results in [45] and the sharp discontinuity in density is maintained.

	$\rho$	$p$	$\mathbf{v}$	$A$	$\mathbf{J}$
$x < 0.05$	1.3333	$1.5 \times 10^5$	$\begin{pmatrix} 35.35\sqrt{10} & 0 & 0 \end{pmatrix}$	$\left( \frac{1.3333}{1.18} \right)^{\frac{1}{3}} I_3$	$\mathbf{0}$
$0.05 \leq x < 0.4$	1	$10^5$	$\mathbf{0}$	$\left( \frac{1}{1.18} \right)^{\frac{1}{3}} I_3$	$\mathbf{0}$
$0.4 \leq x < 0.6$	0.1379	$10^5$	$\mathbf{0}$	$\left( \frac{0.1379}{0.163} \right)^{\frac{1}{3}} I_3$	$\mathbf{0}$
$0.6 \leq x \leq 1$	1	$10^5$	$\mathbf{0}$	$\left( \frac{1}{1.18} \right)^{\frac{1}{3}} I_3$	$\mathbf{0}$

Table 2: Initial conditions for the helium bubble test

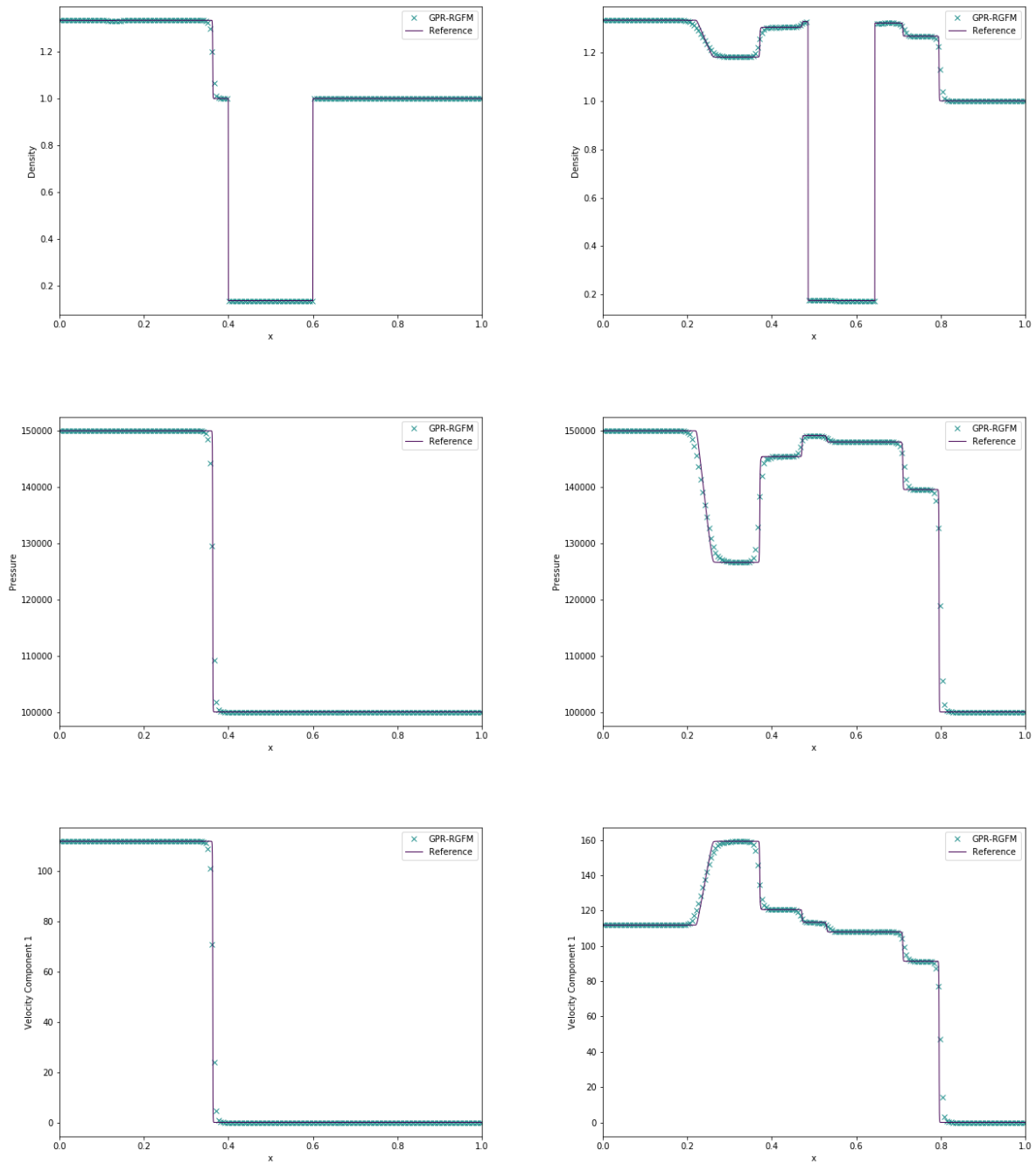


Figure 7: Density, pressure, and velocity for the helium bubble test with GPR-RGFM at times  $t = 7 \times 10^{-4}$  (left) and  $t = 14 \times 10^{-4}$  (right)

	$\rho$	$p$	$\mathbf{v}$	$A$	$\mathbf{J}$
$0 \leq x < 0.7$	1000	$10^9$	$\mathbf{0}$	$I_3$	$\mathbf{0}$
$0.7 \leq x \leq 1$	50	$10^5$	$\mathbf{0}$	$\sqrt[3]{50} \cdot I_3$	$\mathbf{0}$

Table 3: Initial conditions for the water-air shock tube test

### 3.2. Water-Air Shock Tube

This test comprises an interface between water and air, with initial data taken from Chinnayya et al. [10] (see Table 3 on page 21). The aim of this test is to evaluate the ability of the GPR-RGFM at capturing interfaces between qualitatively different fluids. The water is initially at high pressure, and the air at atmospheric pressure. Due to the large difference in state variables and qualitative characteristics of the two fluids, this is an example of a test with which the original GFM for the Euler equations does not perform well.

The results using the GPR-RGFM with 200 cells are shown in Figure 8 on page 22, along with the exact solution to the Euler equations. As can be seen, the material interface is captured well, with the correct intermediate density found by the numerical method.

### 3.3. PBX9404-Copper Shock Tube

This test is taken from [7], with the aim of testing the ability of the GPR-RGFM to model interfaces between fluids and solids. High pressure, reacted PBX9404 is in contact with copper at position  $x = 0.5$  on domain  $x \in [0, 1]$ , with both materials initially at rest. The pressure of the PBX is initially  $18.9GPa$ , and the entropy of the copper is initially 0. The PBX follows an ideal gas EOS, with parameters  $\rho_0 = 1840$ ,  $\gamma = 2.85$ ,  $b_0 = 1$ ,  $\mu = 10^{-2}$ . The copper follows the Godunov-Romenski EOS, with parameters  $\rho_0 = 8930$ ,  $c_v = 390$ ,  $T_0 = 300$ ,  $c_0 = 3939$ ,  $\alpha = 1$ ,  $\beta = 3$ ,  $\gamma = 2$ ,  $b_0 = 2141$ . The test is run until time  $t = 0.5 \times 10^{-6}$ , using 500 cells.

The exact solution to this test is calculated using the iterative solver described in [6]. Plots for density, velocity, and total stress are given in Figure 9 on page 23. As can be seen, the GPR-RGFM is able to reproduce the solution to high fidelity, with a perfectly sharp discontinuity in the density, and a very well resolved discontinuity in the total stress.

### 3.4. Aluminium in Vacuum

This test is taken from [4]. The initial conditions of the test consist of a slab of aluminium, initially with velocity  $\begin{pmatrix} 2 & 0 & 0.1 \end{pmatrix}$ , meeting a vacuum at point  $x = 0.5$ , on the domain  $x \in [0, 1]$ . The distortion of the aluminium is initially given by:

$$A = \begin{pmatrix} 1 & 0 & 0 \\ -0.01 & 0.95 & 0.02 \\ -0.015 & 0 & 0.9 \end{pmatrix}^{-1} \quad (76)$$

The initial density of the aluminium is thus given as  $\rho = \rho_0 \det(A)$ . The aluminium is modeled using the Godunov-Romenski EOS, with parameters  $\rho_0 = 2.71$ ,  $c_v = 9 \times 10^{-4}$ ,  $T_0 = 300$ ,  $c_0 = 5.037$ ,  $\alpha = 1$ ,  $\beta = 3.577$ ,  $\gamma = 2.088$ ,  $b_0 = 3.16$ ,  $c_t = 2$ ,  $\kappa = 204$ .

The test was run until time  $t = 0.06$ , using 500 cells. The results of solving this problem with the GPR-RGFM, not including thermal conduction (as in [4]), are given in Figure 10 on page 25. The results of solving the problem, including thermal conduction, are given in Figure 11 on page 26. As can be seen, in both cases, the GPR-RGFM is able to accurately capture the longitudinal wave and the two transverse

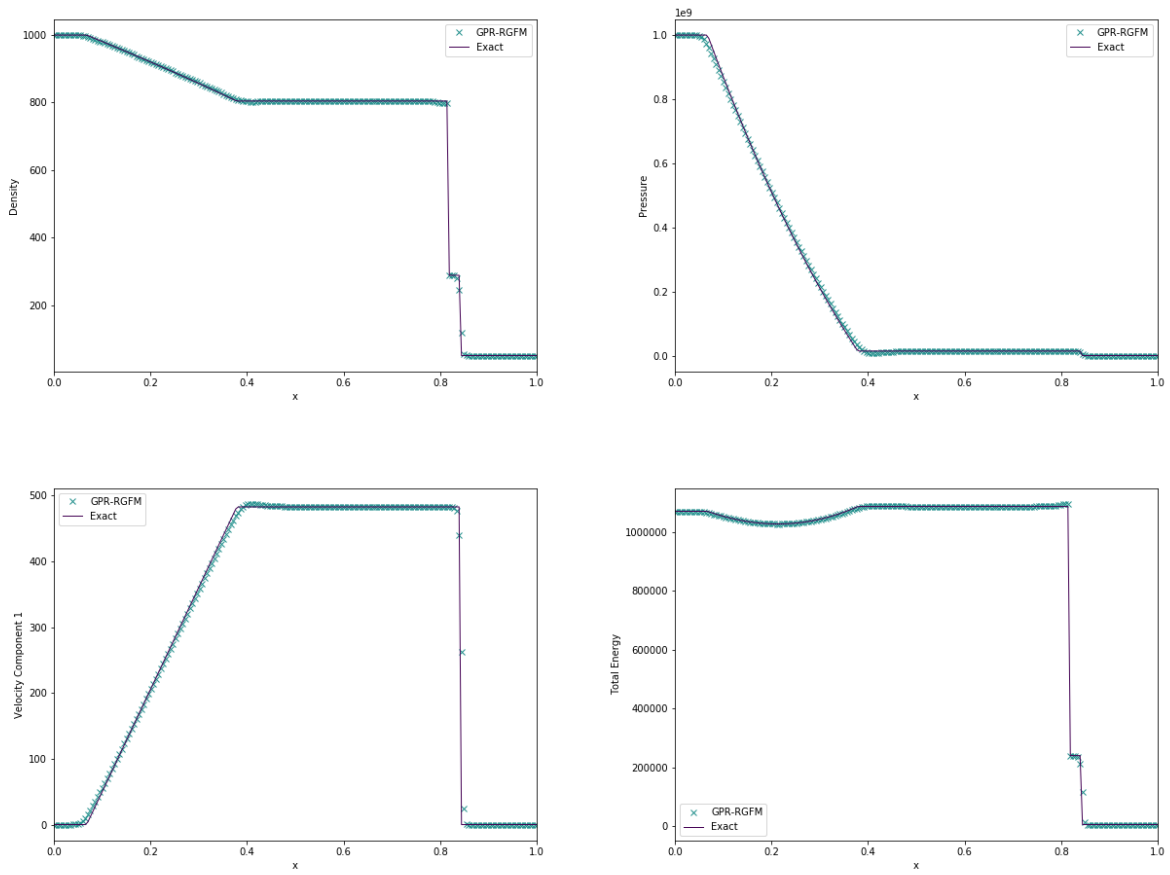


Figure 8: Density, pressure, velocity, and internal energy for the water-air shock tube test with GPR-RGFM

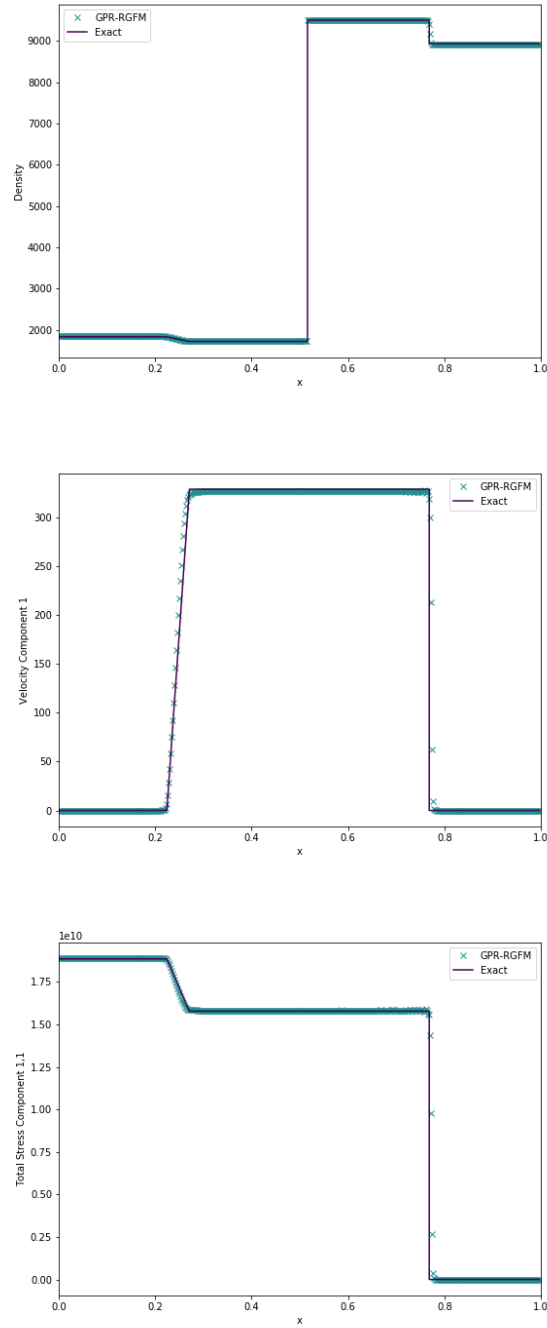


Figure 9: Density, velocity, and total stress for the Copper-PBX test with GPR-RGFM

	$\rho$	$p$	$\mathbf{v}$	$A$	$\mathbf{J}$
$x < 0$	2	1	$\mathbf{0}$	$\sqrt[3]{2} \cdot I_3$	$\mathbf{0}$
$x \geq 0$	0.5	1	$\mathbf{0}$	$\frac{1}{\sqrt[3]{2}} \cdot I_3$	$\mathbf{0}$

Table 4: Initial conditions for the heat conduction test

shock waves that propagate to the left side of the initial point of contact. Without thermal conduction, the interface suffers from a “heating error” of the same kind discussed in [4], manifesting itself as a slight undershoot in the density of the metal at the interface. Note that by incorporating thermal conduction into the numerical method, this heating error completely disappears, without the use of an entropy fix (as in [4]). It must be noted that, in this case, the waves in the state variables now appear to be slightly more diffused than the reference solution. This is the expected effect of incorporating the phenomenon of thermal conduction into this physical problem.

### 3.5. Heat Conduction in a Gas

This test is based on the Heat Conduction in a Gas Test of Dumbser et al. [12]. Two ideal gases at different temperatures are initially in contact at position  $x = 0$ . The initial conditions for this problem are given in Table 4 on page 24.

The material parameters are taken to be:  $\gamma = 1.4$ ,  $c_v = 2.5$ ,  $\rho_0 = 1$ ,  $p_0 = 1$ ,  $c_s = 1$ ,  $c_t = 1$ ,  $\mu = 10^{-2}$ ,  $\kappa = 10^{-2}$ . An interface is initially placed between the two volumes of air at  $x = 0.5$ . The final time is taken to be  $t = 1$ , and 200 cells are used. Results are displayed in Figure 12 on page 27, using the results from [12] as a reference. The material interface is denoted by a dashed vertical line.

The temperature curve generated using the GPR-RGFM matches very well the reference solution. The interface has moved to  $x = 0.53756$ , as is to be expected, as the cooler gas on the left expands as it heats up, and the hotter gas on the right contracts as it cools. Initially, the mass of the left volume is 1 and the right volume is 0.25. At  $t = 1$ , these masses are 0.9997 and 0.2503, respectively. Thus, mass on either side is conserved to a good approximation. Although the GPR-RGFM results for the heat flux match the reference solution well over most of the domain, there are aberrations in a small region around the interface. Although this doesn’t affect the temperature curve, these discrepancies are undesirable, and possible methods to rectify them are discussed in Chapter ??.

### 3.6. Intermaterial Heating-Induced Acoustic Wave

The test assesses the ability of the GPR-RGFM to conduct heat between two different materials. Take the material parameters for air and helium from Section 3.1. Take the scaled spatial variable  $x^*$  defined by:

$$x = \frac{\mu^{air} c_0^{air}}{p_0 \gamma^{air}} x^* \quad (77)$$

The domain  $x^* \in [0, 90]$  is used. Thermal energy is added at the left boundary at a high power of  $\frac{\gamma^{air} p_0 c_0^{air}}{P_r^{air} (\gamma^{air} - 1)}$  (around  $1.7 \times 10^8 W m^{-2}$ ). Three scenarios are tested:

1. The domain is filled with air.
2. The domain comprises two volumes of air, initially separated at  $x^* = 22.5$ .
3. The domain comprises a volume of air (left) and a volume of helium (right), initially separated at  $x^* = 22.5$ .



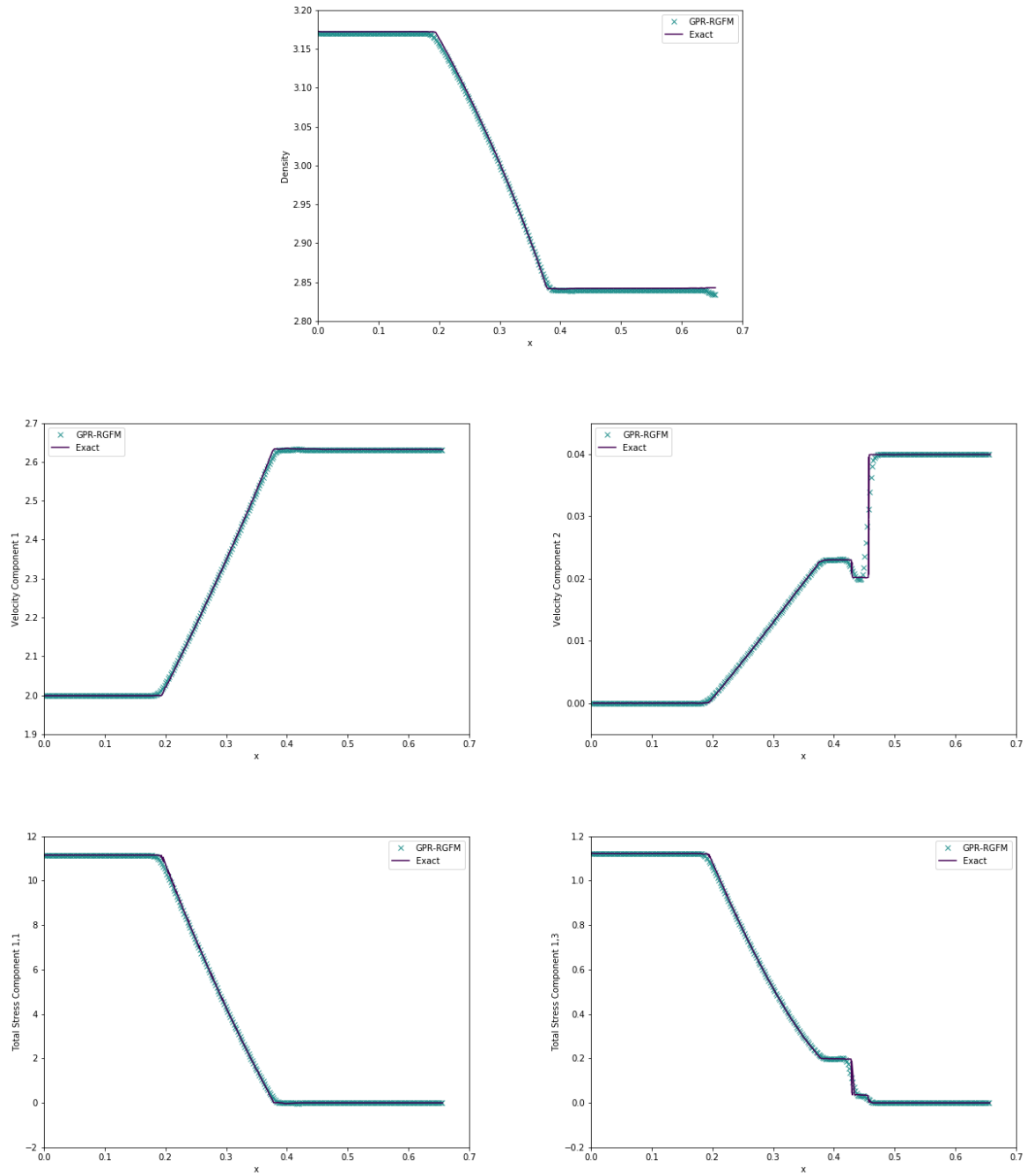


Figure 10: Density, velocity, and total stress for the aluminium-vacuum test with GPR-RGFM, not including thermal conduction

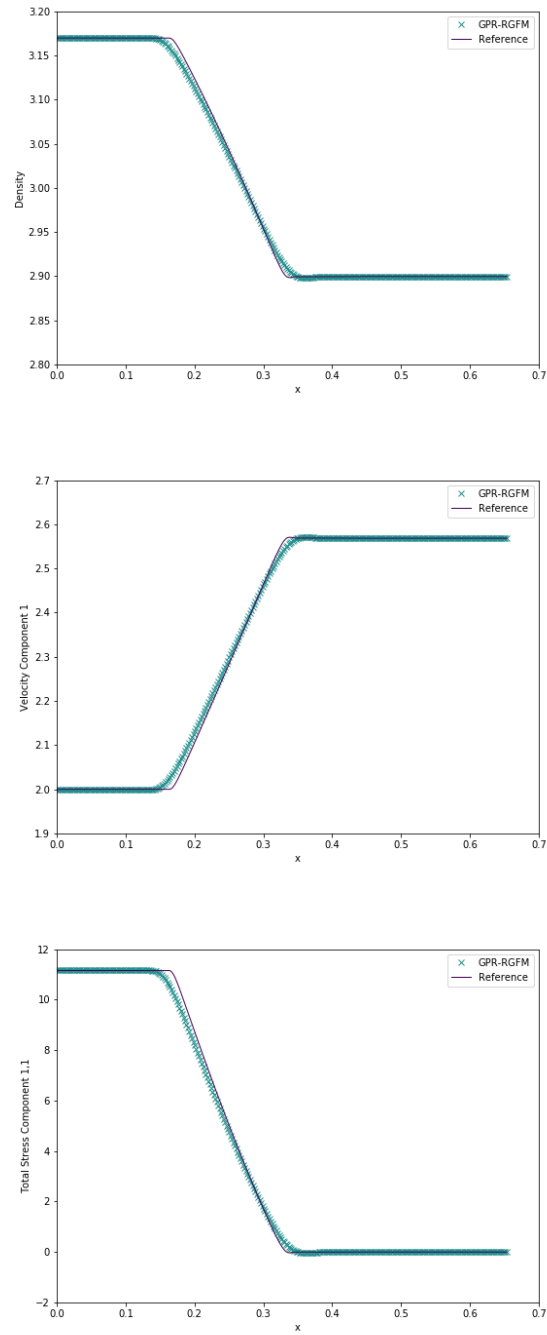


Figure 11: Density, velocity, and total stress for the aluminium-vacuum test with GPR-RGFM, including thermal conduction

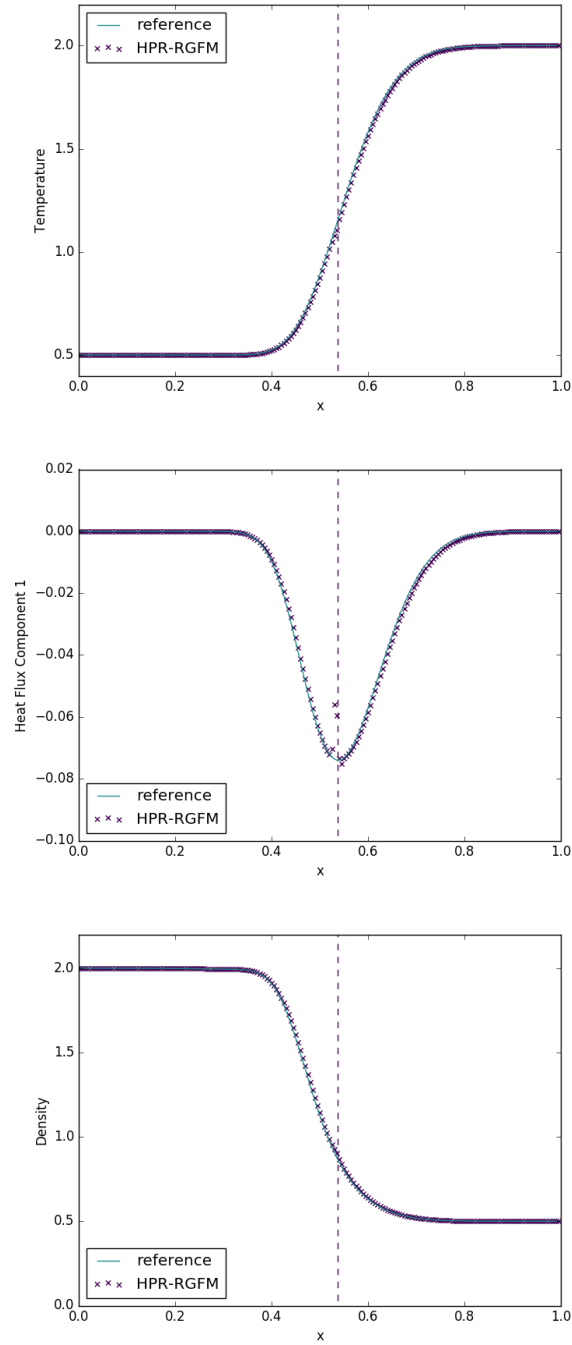


Figure 12: Temperature, heat flux, and density for the intermaterial heat conduction test with GPR-RGFM

	$\rho$	$p$	$\mathbf{v}$	$A$	$\mathbf{J}$
air	1.18	101325	$\mathbf{0}$	$I_3$	$\mathbf{0}$
helium	0.164	101325	$\mathbf{0}$	$I_3$	$\mathbf{0}$

Table 5: Initial conditions for the intermaterial heating-induced acoustic wave test

The initial conditions for the two gases in all scenarios are given in Table 5 on page 28. The results of the test are shown in Figure 13 on page 29 and Figure 14 on page 30 for various times. The material interface is represented by a dashed vertical line in scenarios 2 and 3. All simulations used 400 cells.

As the left wall heats up, a temperature gradient develops and the acoustic wave described appears. The results for scenarios 1 and 2 are indistinguishable, as they should be, and there are no aberrations around the material interface in scenario 2. In scenario 3, the acoustic wave hits the interface at around  $t = 2 \times 10^{-9}$  and then speeds up (as it should, the speed of sound in helium being around three times that of air). The heat flux wave increases in intensity after passing into the helium, owing to the fact that the wave is traveling faster. As expected, all variables displayed are continuous across the interface.

In scenarios 2 and 3 the interface moves to the right as the air heats up and expands. The masses of the air volumes in these two scenarios at various times are given in Table 6 on page 28, demonstrating that mass is conserved well as the interface moves.

Time ( $\times 10^{-9}$ )	0	1	2	3	4	5
Mass in Scenario 2 ( $\times 10^{-6}$ )	1.254	1.255	1.253	1.252	1.252	1.253
Mass in Scenario 3 ( $\times 10^{-6}$ )	1.254	1.253	1.248	1.254	1.255	1.255

Table 6: Mass of the air volume in scenarios 2 and 3 at various times

### 3.7. Taylor Bar

This follows a similar form to that found in [9, 26]. A bar of aluminium of dimensions  $100 \times 500$  travels towards a solid wall at speed 0.015. The surrounding environment is a vacuum. The aluminium bar is modelled by the shock Mie-Gruneisen equation of state, with parameters  $\rho_0 = 2.785$ ,  $c_v = 9 \times 10^{-4}$ ,  $c_0 = 0.533$ ,  $\Gamma_0 = 2$ ,  $s = 1.338$ . The aluminium also follows a plasticity law with parameters  $b_0 = 0.305$ ,  $\sigma_Y = 0.003$ ,  $\tau_0 = 1$ ,  $n = 20$ . The domain has dimensions  $300 \times 510$ , with  $\Delta x, \Delta y = 1$ .

The density and plastic deformation of the bar at times  $t = 0.0025$  and  $t = 0.005$  are shown in Figure 15 on page 31. Unfortunately there are no experimental results for this test, but the reader is asked to note the good agreement here with the results found in [26]. In that study, the boundary between the bar and the vacuum is captured using a Lagrangian scheme, and it is reassuring that the same behaviour is captured here with a characteristically different numerical method.

### 3.8. Aluminum Plate Impact

This test follows the form found in [29] (based on the original formulation found in [21]). An aluminum projectile impacts upon an aluminum plate at 400. The domain is  $[0, 0.03] \times [0, 0.04]$ , with the projectile initially occupying  $[0.001, 0.006] \times [0.014, 0.026]$ , and the plate occupying  $[0.006, 0.028] \times [0.003, 0.037]$ . We have  $\Delta x, \Delta y = 10^{-4}$ . The surroundings are taken to be a vacuum. The aluminium follows a Godunov-Romenski EOS with parameters  $\rho_0 = 2710$ ,  $c_v = 900$ ,  $T_0 = 300$ ,  $c_0 = 5037$ ,  $\alpha = 1$ ,  $\beta = 3.577$ ,  $\gamma = 2.088$ ,  $b_0 = 3160$ ,  $\sigma_Y = 4 \times 10^8$ ,  $\tau_0 = 1$ ,  $n = 100$ . Gauges are placed initially at  $x = 0.0078125, 0.0114375$ ,

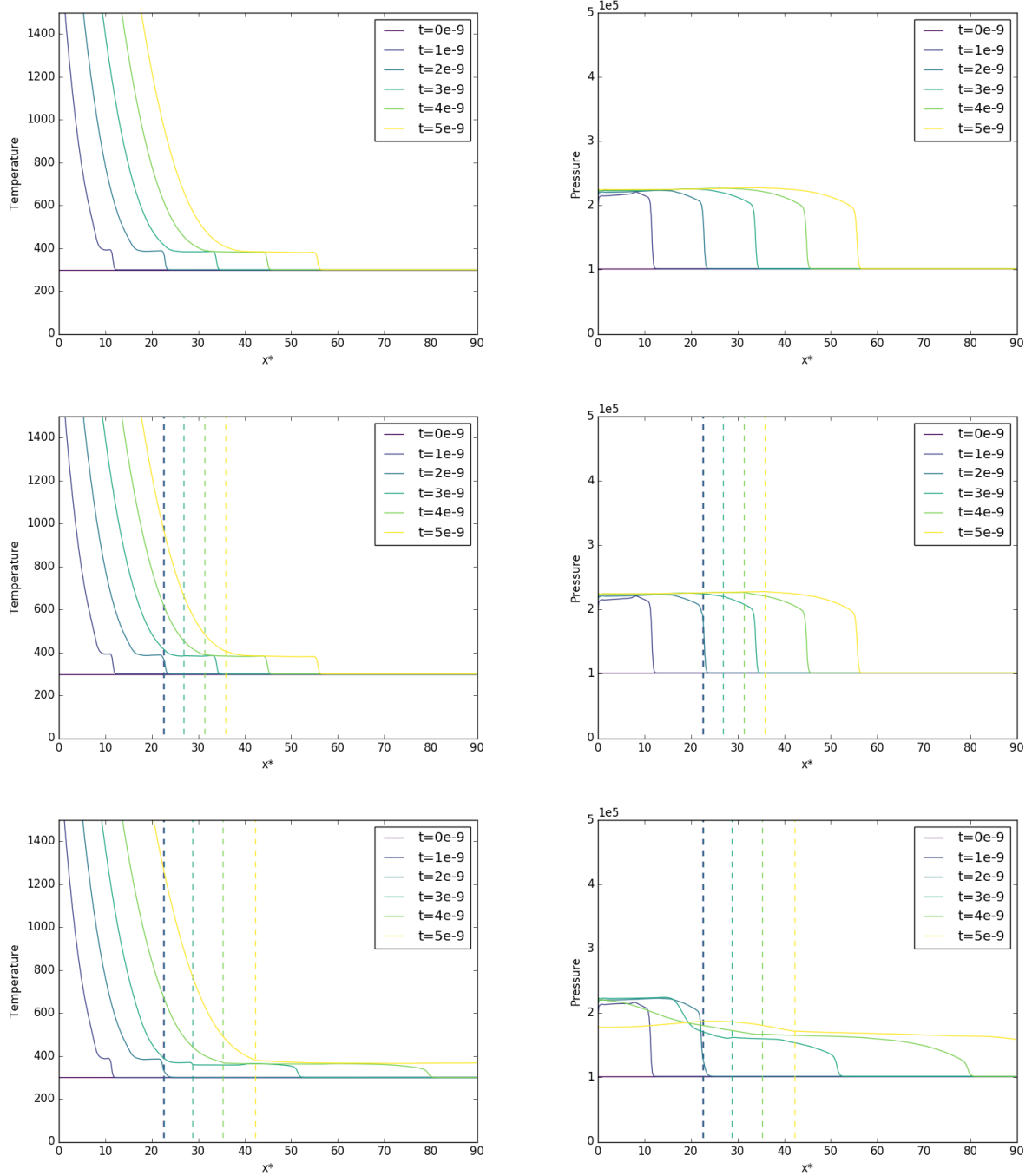


Figure 13: Temperature and pressure for the intermaterial heating-induced acoustic wave test with: a single volume of air (top); two volumes of air initially separated at  $x^* = 22.5$  (middle); air and helium initially separated at  $x^* = 22.5$  (bottom).

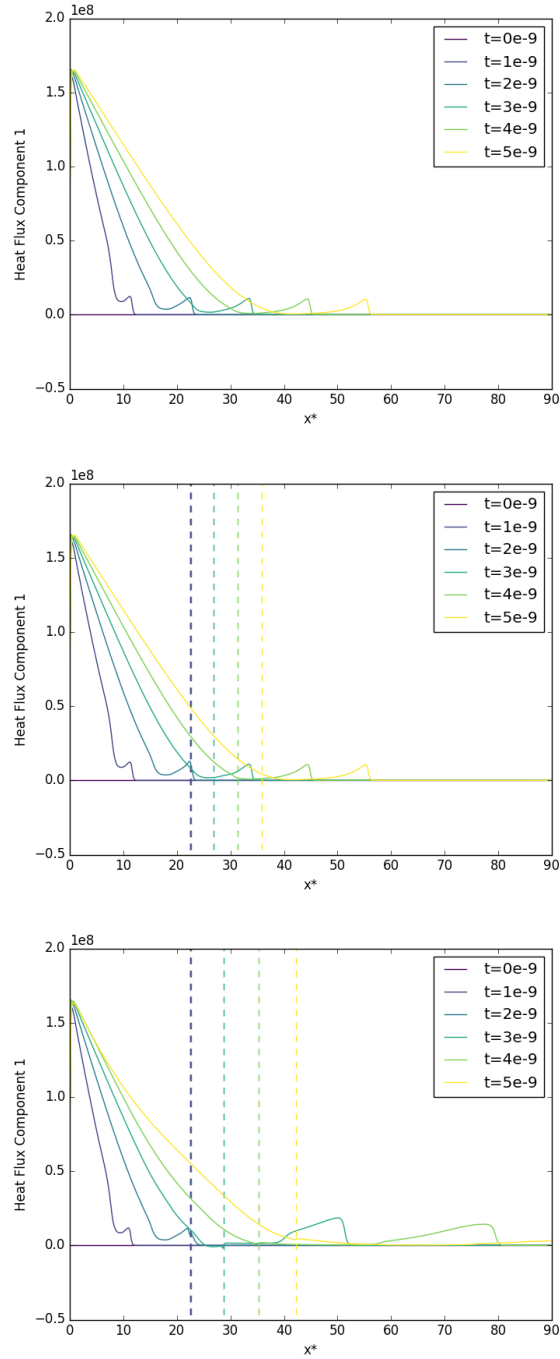


Figure 14: Heat flux for the inter-material heating-induced acoustic wave test with: a single volume of air (top); two volumes of air initially separated at  $x^* = 22.5$  (middle); air and helium initially separated at  $x^* = 22.5$  (bottom).

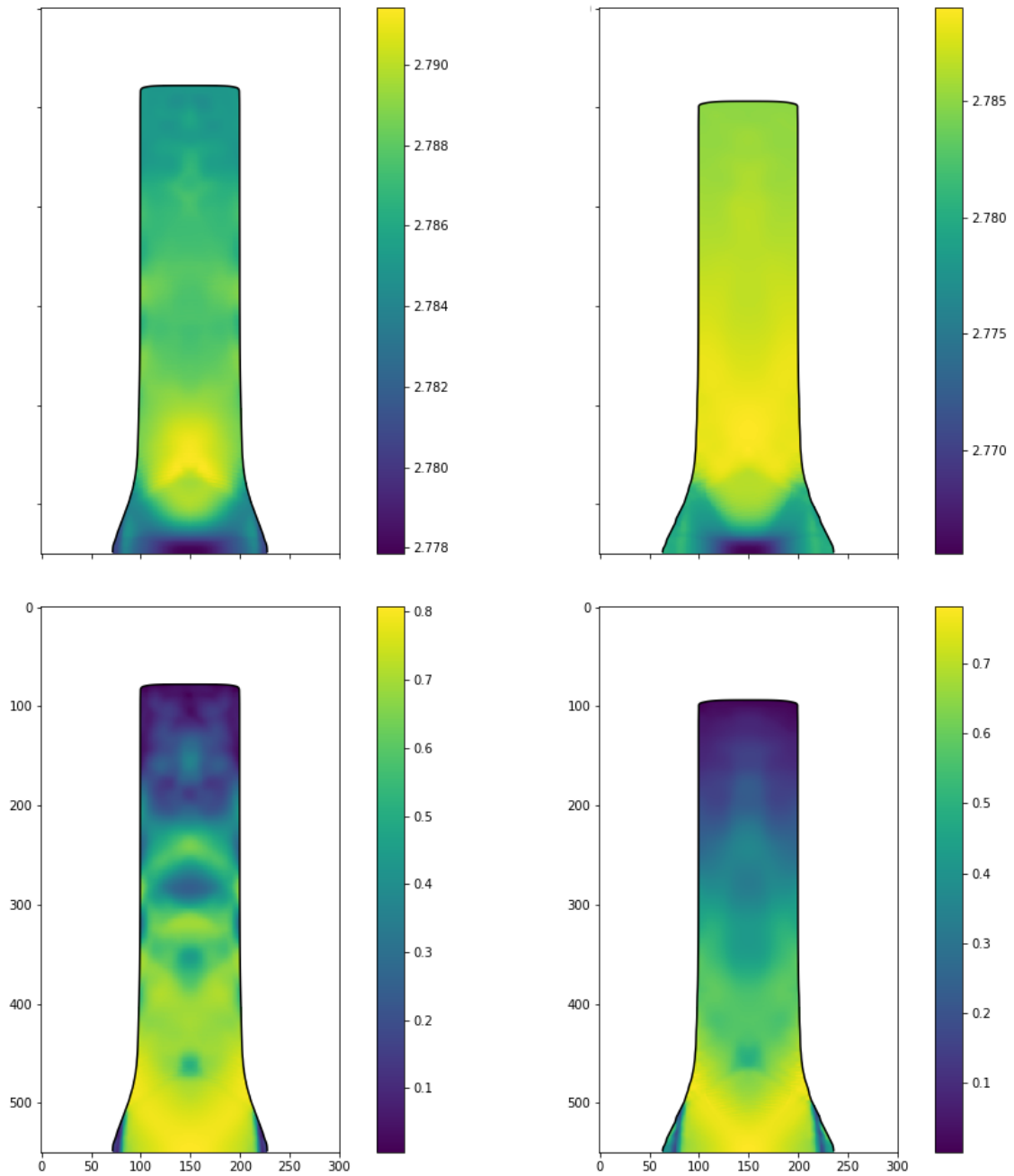


Figure 15: Density (top) and plastic deformation (bottom) for the Taylor bar test, at times  $t = 0.0025$  (left) and  $t = 0.005$  (right)

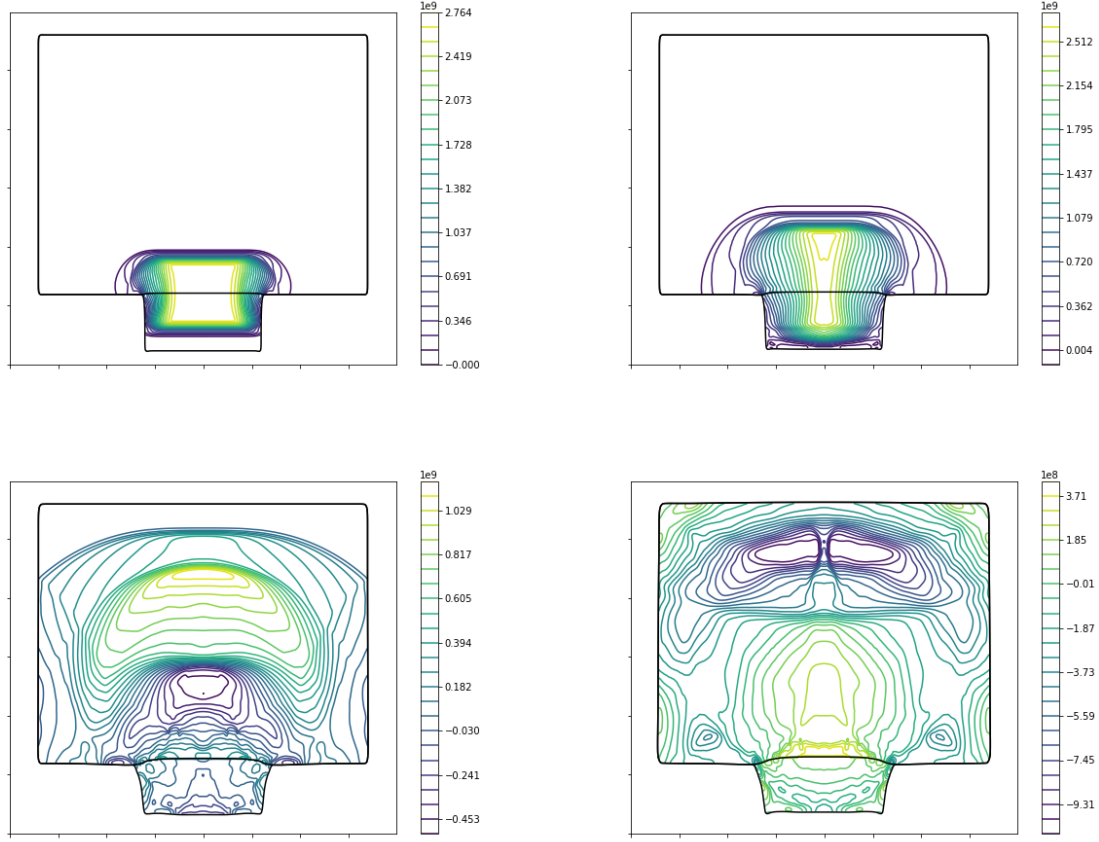


Figure 16: Pressure contour plots for the aluminium plate impact test, at times  $0.5\mu s$ ,  $1\mu s$ ,  $3\mu s$ ,  $5\mu s$

0.0150625, 0.0186875, 0.0223125 to measure the state variables over time, and these gauges are permitted to move with the local velocity of the material. The test is run until time  $t = 5 \times 10^{-6}$ .

The pressure contours throughout the aluminium are shown in Figure 16 on page 32, and plots over time of the  $x$ -velocity, pressure, density, and total stress - as measured by the gauges - are given in Figure 17 on page 33.

#### 4. Discussion

Throughout this study, the various fluids have been assumed to be immiscible. Whilst this is a common assumption in situations where mixing is low or practically non-existent, there are many problems which may require it. It should be fairly straightforward to implement a mixture model such as that proposed by Romenski et al. [36, 35], which uses the same thermal conduction system as the GPR model.

The Riemann Ghost Fluid Method presented in Section 2.2 has been demonstrated to be a viable way of accurately simulating the interfaces between different materials described by the GPR model. Unlike in many existing implementations, heat conduction across the interface was simulated accurately. This greatly simplifies the conceptual framework required for multiphase interactions, as described in 1.1. Implementation should be easier and quicker, and future work can be more focused on a single model, rather than several fundamentally different frameworks.



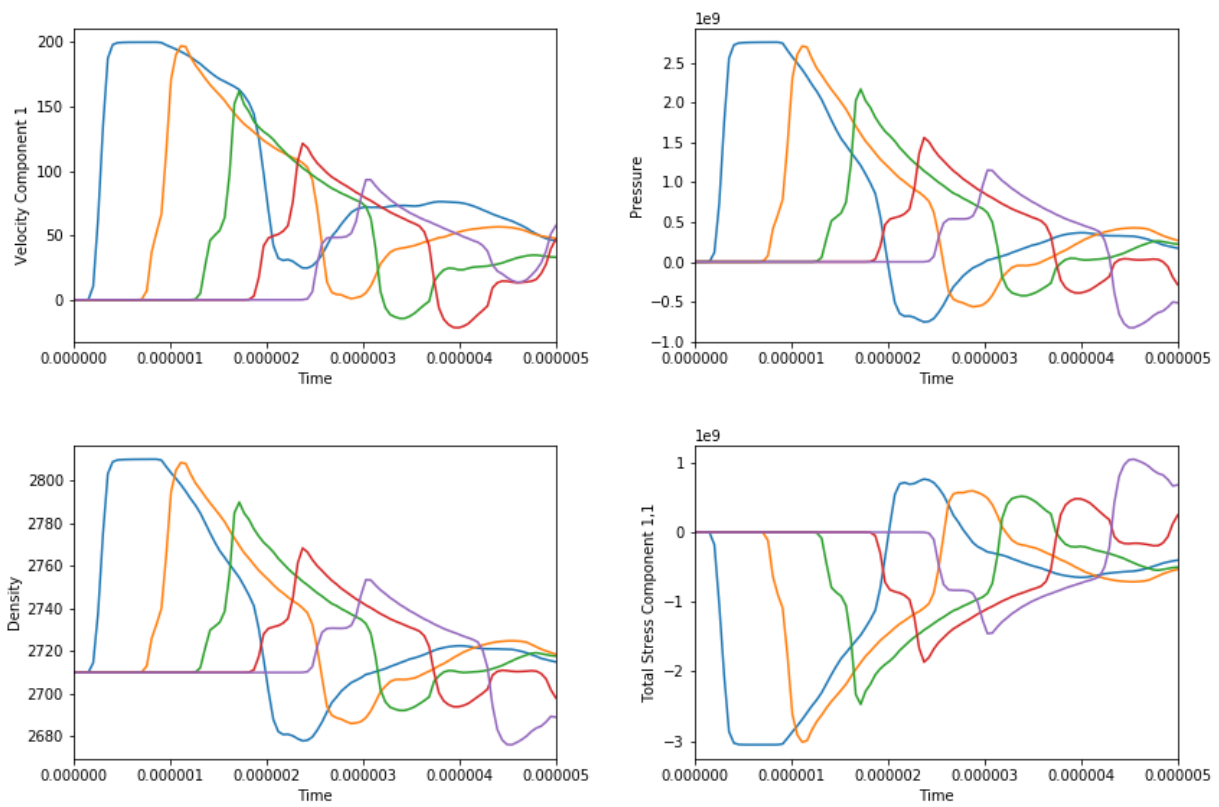


Figure 17:  $x$ -velocity, pressure, density, and total stress over time, as measured by the various gauges of the aluminium plate impact test

#### 4.1. Limitations

The truncation of the Taylor series expansions (49a) and (49b) used to find the star states of the heat flux and the viscous stress tensor implicitly assumes that there are only small differences between the side states and the star states of the variables upon which  $q_1^*$ ,  $\sigma_1^*$  depend ( $\rho$ ,  $p$ ,  $J_1$ , and  $\mathbf{A}_1$ ). If this is the case, higher order terms of the expansion can be neglected. If it is not, however, the method may fail. The linearised nature of the GPR-RGFM solver also implicitly assumes that all waves of interest present in the Riemann Problem are shocks. Thus, strong rarefactions may cause the method to fail.

#### 4.2. Potential Improvements

An obvious improvement to the GPR-RGFM method presented would be to use a better Riemann solver than the iterative, linearised solver devised in Section 2.2. Let  $L$  be the matrix of left eigenvectors of the primitive system. As noted previously, the solver relies upon the fact that each of the following relations holds along the characteristic to which it corresponds:

$$L \cdot \frac{d\mathbf{P}}{dt} = L \cdot \mathbf{S} \quad (78)$$

It may be that some numerical method is required to integrate (78) from the left and right interface boundary states to their respective star states.

Alternatively, a completely different approximate Riemann solver could be employed, such as the universal HLLEM solver of Dumbser et al. [11]. This path-conservative formulation of the HLLEM solver works for general non-conservative systems (such as the GPR model) and is simple to implement. It's based upon a new path-conservative HLL method (building on the original method of Harten, Lax, and van Leer [18]) but is claimed to be able to represent linearly degenerate intermediate waves “with a minimum of smearing” by evaluating the eigenvalues and eigenvectors of the intermediate characteristic fields (given in Section 2.1).

There are iterative exact Riemann solvers for the equations of non-linear elasticity (to which the GPR model reduces as  $\tau_1 \rightarrow \infty$ ). Thus, they will work for applications of the GPR model to solids problems (and perhaps to very viscous fluids problems too). Although these solvers are computationally expensive, they are only used once at each material interface point at each time step, and thus the added accuracy that they provide may be desirable. There are two ways to formulate the equations of non-linear elasticity: one in which the deformation tensor (the analogue of the inverse of the GPR model's distortion tensor) is evolved in time, and one in which its inverse (the analogue of  $A$ ) is evolved instead. Miller's exact solver [31] uses the first formulation and the solver of Barton et al. [5] uses the second. The former can be used to evolve  $A^{-1}$ , from which  $A$  can be calculated. Unfortunately, both solvers critically assume that the source terms of the system vanish, and so are unlikely to produce the correct boundary conditions for the GPR-RGFM when modeling relatively inviscid fluids. It should also be noted that they cannot be used for problems involving heat conduction across material interfaces, and they do not take the thermal conduction subsystem of the GPR model into account.

## 5. References

- [1] M. AIVAZIS, W. GODDARD, D. MEIRON, M. ORTIZ, J. POOL, AND J. SHEPHERD, *A virtual test facility for simulating the dynamic response of materials*, Computing in Science & Engineering, 2 (2000), pp. 39–50.
- [2] F. ALCRUDO AND F. BENKHALDOUN, *Exact solutions to the Riemann problem of the shallow water equations with a bottom step*, Computers & Fluids, 30 (2001), pp. 643–671.
- [3] P. T. BARTON AND D. DRIKAKIS, *An Eulerian method for multi-component problems in non-linear elasticity with sliding interfaces*, Journal of Computational Physics, 229 (2010), pp. 5518–5540.
- [4] P. T. BARTON AND D. DRIKAKIS, *An Eulerian method for multi-component problems in non-linear elasticity with sliding interfaces*, Journal of Computational Physics, 229 (2010), pp. 5518–5540.
- [5] P. T. BARTON, D. DRIKAKIS, E. ROMENSKI, AND V. A. TITAREV, *Exact and approximate solutions of Riemann problems in non-linear elasticity*, Journal of Computational Physics, 228 (2009), pp. 7046–7068.
- [6] ———, *Exact and approximate solutions of Riemann problems in non-linear elasticity*, Journal of Computational Physics, 228 (2009), pp. 7046–7068.
- [7] P. T. BARTON, B. OBADIA, AND D. DRIKAKIS, *A conservative level-set based method for compressible solid/fluid problems on fixed grids*, Journal of Computational Physics, 230 (2011), pp. 7867–7890.
- [8] W. BOSCHERI, M. DUMBSER, AND R. LOUBERE, *Cell centered direct Arbitrary-Lagrangian-Eulerian ADER-WENO finite volume schemes for nonlinear hyperelasticity*, International Journal for Numerical Methods in Fluids, 135 (2016), pp. 111–129.
- [9] W. BOSCHERI, M. DUMBSER, AND R. LOUBERE, *Cell centered direct Arbitrary-Lagrangian-Eulerian ADER-WENO finite volume schemes for nonlinear hyperelasticity*, Computers and Fluids, 134–135 (2016), pp. 111–129.
- [10] A. CHINNAYYA, E. DANIEL, AND R. SAUREL, *Modelling detonation waves in heterogeneous energetic materials*, Journal of Computational Physics, 196 (2004), pp. 490–538.
- [11] M. DUMBSER AND D. S. BALSARA, *A new efficient formulation of the HLLEM Riemann solver for general conservative and non-conservative hyperbolic systems*, Journal of Computational Physics, 304 (2016), pp. 275–319.
- [12] M. DUMBSER, I. PESHKOV, E. ROMENSKI, AND O. ZANOTTI, *High order ADER schemes for a unified first order hyperbolic formulation of continuum mechanics: viscous heat-conducting fluids and elastic solids*, Journal of Computational Physics, 314 (2015), pp. 824–862.
- [13] R. FEDKIW, T. ASLAM, B. MERRIMAN, AND S. OSHER, *A Non-oscillatory Eulerian Approach to Interfaces in Multimaterial Flows (the Ghost Fluid Method)*, Journal of Computational Physics, 152 (1999), pp. 457–492.
- [14] R. P. FEDKIW, *Coupling an Eulerian Fluid Calculation to a Lagrangian Solid Calculation with the Ghost Fluid Method*, Journal of Computational Physics, 175 (2002), pp. 200–224.
- [15] J. FRENKEL, *Kinetic Theory of Liquids*, Oxford University Press, 1947.
- [16] J. GLIMM AND D. MARCHESIN, *A Numerical Method for Two Phase Flow with an Unstable Interface*, Journal of Computational Physics, 39 (1981), pp. 179–200.
- [17] S. K. GODUNOV AND E. I. ROMENSKII, *Nonstationary equations of nonlinear elasticity theory in eulerian coordinates*, Journal of Applied Mechanics & Technical Physics, 13 (1974), pp. 868–884.
- [18] A. HARTEN, P. D. LAX, AND B. VAN LEER, *On Upstream Differencing and Godunov-Type Schemes for Hyperbolic Conservation Laws*, SIAM Review, 25 (1983), pp. 35–61.
- [19] C. W. HIRT AND B. D. NICHOLS, *Volume of fluid (VOF) method for the dynamics of free boundaries*, Journal of Computational Physics, 39 (1981), pp. 201–225.
- [20] G. HOU, J. WANG, AND A. LAYTON, *Numerical methods for fluid-structure interaction - A review*, Communications in Computational Physics, 12 (2012), pp. 337–377.
- [21] B. HOWELL AND G. BALL, *A Free-Lagrange Augmented Godunov Method for the Simulation of Elastic-Plastic Solids*, Journal of Computational Physics, 175 (2002), pp. 128–167.
- [22] B. HÜBNER, E. WALHORN, AND D. DINKLER, *A monolithic approach to fluid-structure interaction using space-time finite elements*, Computer Methods in Applied Mechanics & Engineering, 193 (2004), pp. 2087–2104.
- [23] A. LEGAY, J. CHessa, AND T. BELYTSCHKO, *An Eulerian-Lagrangian method for fluid-structure interaction based on level sets*, Computer Methods in Applied Mechanics & Engineering, 195 (2006), pp. 2070–2087.
- [24] T. G. LIU, B. C. KHOO, AND K. S. YEO, *Ghost fluid method for strong shock impacting on material interface*, Journal of Computational Physics, 190 (2003), pp. 651–681.
- [25] T.-P. LIU, *The Riemann problem for general systems of conservation laws*, Journal of Differential Equations, 18 (1975), pp. 218–234.
- [26] P. H. MAIRE, R. ABGRALL, J. BREIL, R. LOUBERE, AND B. REBOURCET, *A nominally second-order cell-centered Lagrangian scheme for simulating elastic-plastic flows on two-dimensional unstructured grids*, Journal of Computational Physics, 235 (2013), pp. 626–665.
- [27] A. N. MALYSHEV AND E. I. ROMENSKI, *Hyperbolic Equations for Heat Transfer. Global Solvability of the Cauchy Problem*, Sibirskii Matematicheskii Zhurnal, 27 (1984), pp. 128–134.
- [28] L. MICHAEL AND N. NIKIFORAKIS, *Coupling of elastoplastic solid models with condensed-phase explosives formulations*, (submitted), (2016).
- [29] L. MICHAEL AND N. NIKIFORAKIS, *A multi-physics methodology for the simulation of reactive flow and elastoplastic structural response*, Journal of Computational Physics, 367 (2018), pp. 1–27.
- [30] C. MICHLER, S. J. HULSHOFF, E. H. VAN BRUMMELEN, AND R. DE BORST, *A monolithic approach to fluid-structure interaction*, Computers & Fluids, 33 (2004), pp. 839–848.

- [31] G. H. MILLER, *An iterative Riemann solver for systems of hyperbolic conservation laws, with application to hyperelastic solid mechanics*, Journal of Computational Physics, 193 (2004), pp. 198–225.
- [32] S. OSHER AND R. FEDKIW, *Level Set Methods and Dynamic Implicit Surfaces*, Springer, 2002.
- [33] I. PESHKOV AND E. ROMENSKI, *A hyperbolic model for viscous Newtonian flows*, Continuum Mechanics & Thermodynamics, 28 (2016), pp. 85–104.
- [34] F. D. PIN, S. IDELSOHN, E. ONATE, AND R. AUBRY, *The ALE/Lagrangian Particle Finite Element Method: A new approach to computation of free-surface flows and fluid-object interactions*, Computers & Fluids, 36 (2007), pp. 27–38.
- [35] E. ROMENSKI, D. DRIKAKIS, AND E. TORO, *Conservative models and numerical methods for compressible two-phase flow*, Journal of Scientific Computing, 42 (2010), pp. 68–95.
- [36] E. ROMENSKI, A. D. RESNYANSKY, AND E. F. TORO, *Conservative Hyperbolic Formulation for Compressible Two-Phase Flow with Different Phase Pressures and Temperatures*, Quarterly of Applied Mathematics, 65 (2007), pp. 259–279.
- [37] E. I. ROMENSKI, *Hyperbolic Equations of Maxwell’s Nonlinear Model of Elastoplastic Heat-Conducting Media*, Sibirskii Matematicheskii Zhurnal, 30 (1988), pp. 135–159.
- [38] R. ROSSI AND E. ONATE, *Analysis of some partitioned algorithms for fluid-structure interaction*, Engineering Computations, 27 (2010), pp. 20–56.
- [39] P. B. RYZHAKOV, R. ROSSI, S. R. IDELSOHN, AND E. ONATE, *A monolithic Lagrangian approach for fluid-structure interaction problems*, Computational Mechanics, 46 (2010), pp. 883–899.
- [40] S. K. SAMBASIVAN AND H. S. UDAYKUMAR, *Ghost Fluid Method for Strong Shock Interactions Part 1: Fluid-Fluid Interfaces*, AIAA Journal, 47 (2009), pp. 2907–2922.
- [41] ———, *Ghost Fluid Method for Strong Shock Interactions Part 2: Immersed Solid Boundaries*, AIAA Journal, 47 (2009), pp. 2923–2937.
- [42] S. SCHOCH, K. NORDIN-BATES, AND N. NIKIFORAKIS, *An Eulerian algorithm for coupled simulations of elastoplastic-solids and condensed-phase explosives*, Journal of Computational Physics, 252 (2013), pp. 163–194.
- [43] E. F. TORO, *Riemann Solvers and Numerical Methods for fluid dynamics*, vol. 40, 2009.
- [44] E. F. TORO, *Riemann Solvers and Numerical Methods for Fluid Dynamics: A Practical Introduction*, Springer, 2009.
- [45] S. P. WANG, M. H. ANDERSON, J. G. OAKLEY, M. L. CORRADINI, AND R. BONAZZA, *A thermodynamically consistent and fully conservative treatment of contact discontinuities for compressible multicomponent flows*, Journal of Computational Physics, 195 (2004), pp. 528–559.

## 6. Appendix

Taking the ordering  $\mathbf{P}$  of primitive variables in (91), note that (1e), (1b), (1c), (1d) can be stated as:

$$\frac{D\rho}{Dt} + \rho \frac{\partial v_k}{\partial x_k} = 0 \quad (79a)$$

$$\frac{Dv_i}{Dt} + \frac{1}{\rho} \frac{\partial \Sigma_{ik}}{\partial x_k} = 0 \quad (79b)$$

$$\frac{DA_{ij}}{Dt} + A_{ik} \frac{\partial v_k}{\partial x_j} = -\frac{\psi_{ij}}{\theta_1} \quad (79c)$$

$$\frac{DJ_i}{Dt} + \frac{1}{\rho} \frac{\partial T \delta_{ik}}{\partial x_k} = -\frac{H_i}{\theta_2} \quad (79d)$$

$$\frac{DE}{Dt} + \frac{1}{\rho} \frac{\partial (\Sigma_{ik} v_i + T H_k)}{\partial x_k} = 0 \quad (79e)$$

where the total stress tensor  $\Sigma = pI + \rho A^T \psi$ . Note that:

$$\begin{aligned} \frac{DE}{Dt} &= \frac{\partial E}{\partial p} \frac{Dp}{Dt} + \frac{\partial E}{\partial \rho} \frac{D\rho}{Dt} + v_i \frac{Dv_i}{Dt} + \frac{\partial E}{\partial A_{ij}} \frac{DA_{ij}}{Dt} + H_i \frac{DJ_i}{Dt} \\ &= \frac{\partial E}{\partial p} \frac{Dp}{Dt} - \rho \frac{\partial E}{\partial \rho} \frac{\partial v_k}{\partial x_k} - \frac{1}{\rho} v_i \frac{\partial \Sigma_{ik}}{\partial x_k} - \frac{\partial E}{\partial A_{ij}} \left( A_{ik} \frac{\partial v_k}{\partial x_j} + \frac{\psi_{ij}}{\theta_1} \right) - H_i \left( \frac{1}{\rho} \frac{\partial T \delta_{ik}}{\partial x_k} + \frac{H_i}{\theta_2} \right) \end{aligned} \quad (80)$$

Thus, the energy equation becomes:

$$\frac{\partial E}{\partial p} \frac{Dp}{Dt} - \rho \frac{\partial E}{\partial \rho} \frac{\partial v_k}{\partial x_k} - \frac{1}{\rho} v_i \frac{\partial \Sigma_{ik}}{\partial x_k} - \frac{\partial E}{\partial A_{ij}} A_{ik} \frac{\partial v_k}{\partial x_j} - \frac{H_k}{\rho} \frac{\partial T}{\partial x_k} + \frac{1}{\rho} \frac{\partial (\Sigma_{ik} v_i + T H_k)}{\partial x_k} = \frac{\partial E}{\partial A_{ij}} \frac{\psi_{ij}}{\theta_1} + \frac{H_i H_i}{\theta_2} \quad (81)$$

Simplifying:

$$\frac{Dp}{Dt} + \frac{1}{\rho E_p} \left( \Sigma_{ik} - \rho A_{ji} \frac{\partial E}{\partial A_{jk}} - \rho^2 \frac{\partial E}{\partial \rho} \delta_{ik} \right) \frac{\partial v_i}{\partial x_k} + \frac{T}{\rho E_p} \frac{\partial H_k}{\partial x_k} = \frac{\partial E}{\partial A_{ij}} \frac{\psi_{ij}}{\theta_1 E_p} + \frac{H_i H_i}{\theta_2 E_p} \quad (82)$$

We have<sup>567</sup>:

$$\frac{p - \rho^2 E_p}{\rho E_p} = \rho c_0^2 \quad (87a)$$

$$\frac{c_t^2 T}{\rho E_p} = \frac{\rho c_h^2}{T_p} \quad (87b)$$

$$\left. \frac{\partial E}{\partial A} \right|_{\rho, p} = \left( 1 - 2\rho^2 E_p \frac{\partial \log(c_s)}{\partial \rho} \right) \psi \quad (87c)$$

$$-\rho A^T \left. \frac{\partial E}{\partial A} \right|_{\rho, p} = \sigma + \rho^2 E_p \left( \frac{\sigma}{\rho} - \frac{\partial \sigma}{\partial \rho} \right) \quad (87d)$$

The full system then becomes:

---

5

$$\begin{aligned} \frac{p - \rho^2 E_p}{\rho E_p} &= \frac{\rho^2 E_p|_s - \rho^2 E_p|_p}{\rho E_p|_\rho} = \rho \frac{E_p|_s - (E_p|_s + E_s|_\rho s_\rho|_p)}{E_s|_\rho s_\rho|_\rho} \\ &= \rho \frac{-s_\rho|_p}{s_p|_\rho} = \rho \left. \frac{\partial p}{\partial \rho} \right|_s \end{aligned} \quad (83)$$

6

$$\frac{c_t^2 T}{\rho E_p} = \frac{c_t^2 T}{\rho c_v T_p} = \frac{\rho c_h^2}{T_p} \quad (84)$$

7

$$\left. \frac{\partial E}{\partial A} \right|_{\rho, p} = \left( c_s^2 - \frac{\rho}{\Gamma} \frac{\partial c_s^2}{\partial \rho} \right) \frac{\psi}{c_s^2} = \left( 1 - 2 \frac{\rho^2}{\rho \Gamma} \frac{\partial \log(c_s)}{\partial \rho} \right) \psi \quad (85)$$

$$\begin{aligned} \frac{\partial \sigma}{\partial \rho} &= \frac{\partial}{\partial \rho} \left( -\rho c_s^2 A^T \frac{\psi}{c_s^2} \right) = -c_s^2 A^T \frac{\psi}{c_s^2} - \rho \frac{\partial c_s^2}{\partial \rho} A^T \frac{\psi}{c_s^2} \\ &= \frac{\sigma}{\rho} + 2 \frac{\partial \log(c_s)}{\partial \rho} \sigma \end{aligned} \quad (86)$$

$$\frac{D\rho}{Dt} + \rho \frac{\partial v_k}{\partial x_k} = 0 \quad (88a)$$

$$\frac{Dp}{Dt} + \rho c_0^2 \frac{\partial v_i}{\partial x_i} + \left( \sigma_{ik} - \rho \frac{\partial \sigma_{ik}}{\partial \rho} \right) \frac{\partial v_i}{\partial x_k} + \frac{\rho c_h^2}{T_p} \frac{\partial J_k}{\partial x_k} = \left( 1 - 2\rho^2 E_p \frac{\partial \log(c_s)}{\partial \rho} \right) \frac{\|\psi\|_F^2}{\theta_1 E_p} + \frac{\|H\|^2}{\theta_2 E_p} \quad (88b)$$

$$\frac{DA_{ij}}{Dt} + A_{ik} \frac{\partial v_k}{\partial x_j} = -\frac{\psi_{ij}}{\theta_1} \quad (88c)$$

$$\frac{Dv_i}{Dt} - \frac{1}{\rho} \frac{\partial \sigma_{ik}}{\partial \rho} \frac{\partial \rho}{\partial x_k} + \frac{1}{\rho} \frac{\partial p}{\partial x_i} - \frac{1}{\rho} \frac{\partial \sigma_{ik}}{\partial A_{mn}} \frac{\partial A_{mn}}{\partial x_k} = 0 \quad (88d)$$

$$\frac{DJ_i}{Dt} + \frac{T_\rho}{\rho} \frac{\partial \rho}{\partial x_i} + \frac{T_p}{\rho} \frac{\partial p}{\partial x_i} = -\frac{H_i}{\theta_2} \quad (88e)$$

Thus, the GPR system can be written in the following form:

$$\frac{\partial \mathbf{P}}{\partial t} + \mathbf{M} \cdot \nabla \mathbf{P} = \mathbf{S}_p \quad (89)$$

(96)

$$\mathbf{P} = \begin{pmatrix} \rho \\ p \\ A_{11} \\ A_{21} \\ A_{31} \\ A_{12} \\ A_{22} \\ A_{32} \\ A_{13} \\ A_{23} \\ A_{33} \\ v_1 \\ v_2 \\ v_3 \\ J_1 \\ J_2 \\ J_3 \end{pmatrix} \quad (91)$$

$$\mathbf{S}_p = \frac{1}{\theta_1} \begin{pmatrix} 0 \\ \left( \frac{1}{E_p} - 2\rho^2 \frac{\partial \log(c_s)}{\partial p} \right) \|\psi\|_F^2 \\ -\psi_{11} \\ -\psi_{21} \\ -\psi_{31} \\ -\psi_{12} \\ -\psi_{22} \\ -\psi_{32} \\ -\psi_{13} \\ -\psi_{23} \\ -\psi_{33} \\ 0 \\ 0 \\ 0 \\ 0 \\ 0 \\ 0 \\ 0 \end{pmatrix} + \frac{1}{\theta_2} \begin{pmatrix} 0 \\ \frac{1}{E_p} \|\mathbf{H}\|^2 \\ 0 \\ 0 \\ 0 \\ 0 \\ 0 \\ 0 \\ 0 \\ 0 \\ 0 \\ 0 \\ 0 \\ 0 \\ 0 \\ -H_1 \\ -H_2 \\ -H_3 \end{pmatrix} \quad (92)$$